Compressibility-induced destabilisation of falling liquid films: an integral approach

P. Botticini, Gianluca Lavalle, D. Picchi, P. Poesio

Graphical Abstract

Compressibility–induced destabilisation of falling liquid films: an integral approach

P. Botticini, G. Lavalle, D. Picchi, P. Poesio

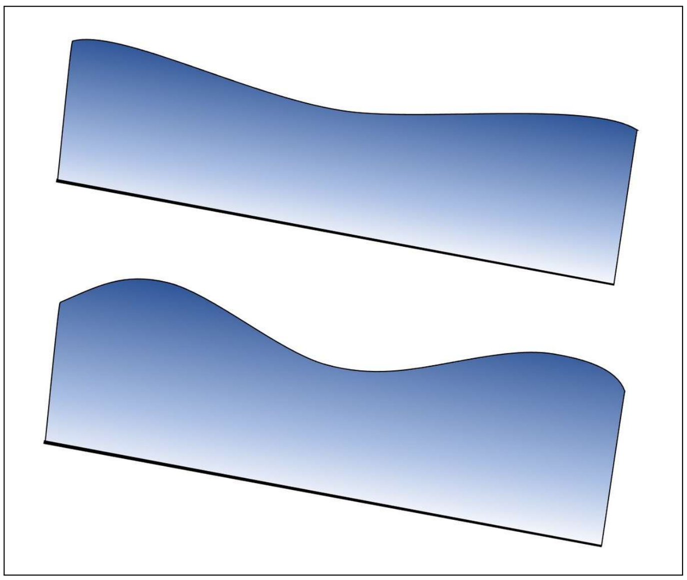

Highlights

Compressibility–induced destabilisation of falling liquid films: an integral approach

P. Botticini, G. Lavalle, D. Picchi, P. Poesio

- We introduced small density variations within a gravity–driven falling film via a barotropic equation of state and investigated how this affects the flow temporal linear stability.
- In the final depth–averaged evolution equations compressibility is reflected in two additional second–order terms.
- A weak compressibility boosts the onset of interfacial instability, especially in low–inertial regimes and along modest slopes.
- We detected an extra flow rate of hydrostatic origin due to compressibility and complemented our analysis with the wave–hierarchy theory.

Compressibility–induced destabilisation of falling liquid films: an integral approach

P. Botticini[a,b], G. Lavalle[a,*], D. Picchi[b], P. Poesio[b]

[a] *Mines Saint–Etienne, Univ. Lyon, CNRS, UMR 5307 LGF, Centre SPIN, F-42023, Saint–Etienne, France*
[b] *Dipartimento di Ingegneria Meccanica e Industriale, Università di Brescia, Via Branze 38, 25123, Brescia, Italy*

Abstract

We revisit the classical 2D problem of a gravity–driven liquid layer down an inclined plate (Kapitza, *Zh. Eksp. Teor. Fiz.*, vol. 18 (1), 1948, pp. 3–28), relaxing the usual assumption of homogeneous fluid. We set out to answer three major issues. When the fluid density is allowed to vary, (i) how does this feature structurally affect the formulation of a low–dimensional depth–averaged model? (ii) To what extent and (iii) by virtue of which physical mechanism does compressibility participate in the long–wave interfacial instability? To provide the relevant answers, (i) we first make use of a second–order asymptotic expansion in the shallowness parameter to develop a weakly–compressible boundary–layer system: starting from a two–equation momentum–integrated model, an additional barotropic equation of state is required for closure purposes. In this respect, (ii) a temporal linear stability analysis is performed: it is revealed that compressibility plays a destabilising role whose magnitude is enhanced at intermediately tilted configurations,

* *Email address:* gianluca.lavalle@emse.fr (G. Lavalle)

and the more the Reynolds number approaches the critical threshold in the incompressible limit. (iii) We finally interpret the ensuing dispersion relation under the convenient framework of two–wave hierarchy, initiated by Whitham (*Linear and Nonlinear Waves*, Wiley—Interscience, 1974): the primary instability gets promoted by the flow compressibility as it contributes to deceleration of dynamic waves most significantly in the low–inertia regime. Indeed, compressibility locally acts as a further boost to the inertia–based mechanism of Kapitza instability by amplifying flow–rate variations within the liquid film.

Keywords: falling liquid films, interfacial instability, low–dimensional models

PACS: 47.15.Cb, 47.20.Ma, 68.15.+e

2000 MSC: 76E17, 76E19, 76M45

1. Introduction

Liquid layers sliding down an incline are routinely encountered in nature and represent a cross–disciplinary and highly topical object of study. Starting with the pioneer studies of Kapitza father–son team (Kapitza, 1948; Kapitza and Kapitza, 1949), visual observations have revealed the development of a wide variety of intriguing patterns along the fluid interface, from simple sinusoidal perturbations to strongly non–periodic three–dimensional solitons (Chang, 1994; Alekseenko et al., 1994).

This issue is also of practical relevance in many biological and industrial processes (Craster and Matar, 2009). Cooling towers, distillation units, multi–phase heat exchangers, fluid–phase separators, jet–film devices, power station condenser tubes, absorption columns, electrolytic cells, scrubbers for pollution abatement, injection systems for enhanced oil recovery, *etc.* all benefit from the strong effect of superficial waves on the underlying processes of heat and mass transfer. For instance, according to data reported by Frisk and Davis (1972), the heat transfer intensification by waves forming along a water film in presence of a co–current air flow attains more than 100 % with respect to the flat–film scenario. On the other hand, for some applications such as coating operations, a uniform flow thickness is required and instabilities should be prevented (Weinstein and Ruschak, 2004).

So far, the majority of works on wavy falling films is performed assuming flow incompressibility, *i.e.* the density of a fluid element remains uniform and constant. However, in many fields of science and engineering, this assumption may constitute an oversimplification of the physical problem, possibly leading to inaccurate conclusions. One example is the transport of carbon dioxide in pipelines from the energy plants to the injection sites for CCUS applications. When supercritical carbon dioxide is employed as solvent or carrier, in fact, density turns out to be an essential parameter in determining the performance of such a technological process. In this context, avoiding the unbounded growth of superficial disturbances, which can result in the emergence of slugs or even structural damages (Lu et al., 2020), is necessary for the safety of the transport infrastructure.

Although the convective long–wave interfacial mode known as Kapitza instability (Kapitza, 1948) constitutes a long–standing knowledge in case of a tilted or vertical plate, a deep understanding of how density variations enter this paradigm is still lacking in the literature. Thus, the link between the compressibility and the occurrence of the Kapitza instability needs to be clarified and has prompted us to address the following question: which are the main implications of density inhomogeneities on the onset of Kapitza instability in inclined falling liquid films?

Recently, the relevance of wavy film flows has led to a number of attempts to achieve models for the evolution of the film thickness and its mean velocity (or flow rate) and to find a compromise between the accuracy and the computational effort. In most cases, the flow description is not too far from its wavy–less configuration, designed as Nusselt state (Nusselt, 1916). This makes the long–wave asymptotic expansion a feasible approach, which forms the cornerstone of many models derived after the influential paper of Benney (1966), who developed an evolution equation for the film height by introducing a small–scale parameter. However, Benney's equation suffers of finite–time blow–up of the time–dependent solution. This problem was addressed by Shkadov (1967) assuming that streamwise variations are small as compared with those developing in the crosswise direction, and through pressure removal boundary layer equations (BLEs) ensue. These are then averaged over the fluid depth to capture the main physical features of the flow by means of integral variables. Nonetheless, Shkadov's system of equations fails in capturing the correct long–wave instability threshold. This issues was addressed by Ruyer-Quil and Manneville (1998, 2000), who introduced the weighted residual integral boundary–layer model (WRIBL) and assured model consistency by formulating a closure law for the wall shear stress.

In this paper, our purpose is to deal with a weakly inhomogeneous medium to investigate whether and how the action of a low compressibility enhances or mitigates the onset of long–wave interfacial instability. We therefore start by applying Benney's modelling strategy to a barotropic flow in a weakly–compressible scenario. We globally characterise it in terms of compressibility by means of the Mach number and formulate a coupled system of two evolution equations by making use of the depth–wise averaging method based on the classical long–wave expansion as in Lavalle et al. (2015, 2017), *i.e.* by integration of the momentum balance (momentum integral method or MIM). The resulting model is comprehensive of second–order viscous diffusion effects, which allow us to achieve good agreement in the incompressible limit in terms of the cut–off wavenumber with the Orr–Sommerfeld solution (Kalliadasis et al., 2013).

Our study focuses on the influence of compressibility on the development of linear surface waves on a liquid film falling down an inclined wall under a shear–free atmosphere (figure 1). For this, we consider the primary instability of the weakly–compressible uniform base flow and solve the temporal stability problem based on the long–wave model equations. By doing this, we answer two additional questions: (i) how does compressibility affect the formulation of depth–integrated equations? (ii) Which physical mechanism does the compressibility trigger in the long–wave interfacial instability?

Behind the usual incompressible way of modelling falling liquid layers, it is assumed that the speed of sound, when compared to the convective velocity scale, is sufficiently high to be considered infinite. Therefore, (i) a unique velocity scale appears in the problem and (ii) the fluid density is uniform and constant. On the contrary, when a finite speed of sound is taken into account, the scenario significantly changes. (i) Convective transport and pressure wave propagation occur at disproportional rates, thereby requiring a proper incorporation of an additional dimensionless group in the problem. In this regard, the Sarrau–Mach number can be used to express the magnitude of the fluid speed as compared to the sound speed within the same medium. In addition, (ii) the fact that density field is allowed to vary in space and time demands the introduction of an Equation of State (EoS) among the governing equations.

Unfortunately, very little attention, to the best of our knowledge, has been up to now devoted to the assessment of the impact of compressibility on the film long–wave instability. In fact, only a few works tried to tackle this issue.

An extension of long–wave models to weakly–compressible barotropic flows is first proposed by Richard (2021). Compressibility–related effects are captured by means of a dedicated Mach number, defined by means of the incompressible surface waves celerity, and, in the limit where the sound speed goes to infinity, the incompressible version of the model is correctly recovered. However, the system of four Favre–averaged equations derived by Richard (2021) is intended for simulation of coastal waves and the author frames his argumentation around the ultimate goal of correctly predicting tsunamis' arrival time. Although the long–wave assumption still holds for a tidal wave in a deep ocean, the relevant spatial scales involved widely differs from the ones we are interested in. Moreover, in Richard (2021), the wave propagation is studied within an inviscid medium, neglecting viscous effects.

Such friction terms have also been neglected in the work of Bresch et al. (2020), who developed an augmented skew–symmetric system of depth–

integral equations with capillarity. Their work aims at ensuring the stability of numerical schemes in presence of large gradients of fluid height or fluid density.

In the context of flows within a narrow interstice formed between two surfaces, Almqvist et al. (2019) consider a class of iso–viscous fluids obeying a constitutive power–law density–pressure relationship. Lubrication theory, scaling and asymptotic analysis are extensively used in that work to show that the degree of compressibility for a thin film flow determines whether the terms governing inertia may or may not be neglected. Notwithstanding the rigorousness of their procedure, the study of a capillary flow is not at all comparable to a free–surface gravity–driven liquid film.

We conclude by recalling the fundamental results regarding the linear stability problem of a falling liquid film in a passive gas or shear–free atmosphere, which is the configuration studied in this work. Benjamin (1957) and Yih (1963) solved the temporal linear stability problem formulated by Orr (1907) and Sommerfeld (1908) in the context of a gravity–driven incompressible film flow. In particular, they detected the long–wave instability threshold in terms of a critical Reynolds number $Re_{cr} = 5/6 \cot\beta$, where β identifies the inclination angle, being the Reynolds number based on the mean film flow velocity. Their analysis reveals that inertia destabilizes long waves and the related mechanism has been explained either through the shift between the vorticity perturbation and the perturbed interface (Kelly et al., 1989; Kalliadasis et al., 2013; Smith, 1990), or via the time lag at which flow rate adapts to its inertialess target value (Dietze, 2016). With the aim to investigate the role of compressibility on the long–wave instability, we follow the latter approach by considering the effect of compressibility on the inertialess flow rate, similarly to Lavalle et al. (2019), who applied the same methodology to explain the confinement–induced stabilisation of falling liquid films. Finally, we complement this analysis by studying the role of compressibility via the two–wave competition theory formulated by Whitham (Whitham, 1974), and employed by Samanta et al. (2011) and Samanta (2014) for liquid films down a slippery inclined plane or for shear-imposed falling films.

Accordingly, the structure of our paper is as follows. Section § 2 contains the basic governing equations, the boundary conditions of the problem, and the definition of the principal dimensionless groups, together with the long–wave scaling. Then, the low–dimensional modelling is discussed in § 3, from the specification of the EoS to the derivation of the weakly–compressible integral model. This will serve in the second part of the manuscript, devoted to the linear temporal stability eigen–problem, whose compatibility yields the dispersion relation outlined in § 4. To follow, § 5 presents our main findings in terms of critical threshold and parametric study of celerity branches. The mechanism governing the influence of compressibility on the film stability is finally elucidated in § 6. Concluding remarks are summarised in § 7, while some details of the analysis that were not included in the main body of the text are given in the appendix for completeness.

2. Flow configuration and theoretical formulation

Herein we consider the two–dimensional compressible flow of a gravity–driven iso–viscous liquid film, falling along a tilted wall within a shear–free atmosphere, as sketched in figure 1. The liquid film is Newtonian.

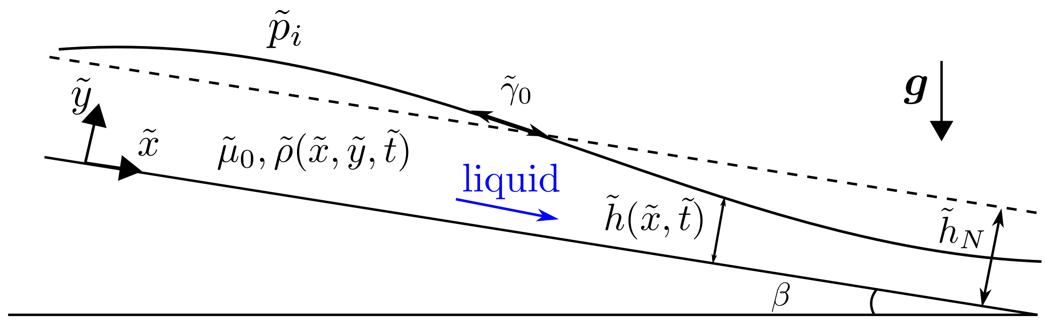

Figure 1: Schematic diagram of the 2D slightly compressible flow of a wavy gravity–driven liquid film with uniform and constant viscosity $\tilde{\mu}_0$ and surface tension $\tilde{\gamma}_0$, exhibiting a non–uniform and variable density $\tilde{\rho}(\tilde{x}, \tilde{y}, \tilde{t})$. The coordinate system is defined by $\langle \tilde{x}, \tilde{y} \rangle$. The fluid layer, of variable thickness $\tilde{h}(\tilde{x}, \tilde{t})$, flows under the action of gravity $\boldsymbol{g}$ along a plate having an inclination angle β with respect to the horizontal direction. $\tilde{h}_N$ refers to Nusselt solution (Nusselt, 1916) and denotes the waveless film thickness. An interfacial constant and uniform normal pressure $\tilde{p}_i$ is present.

$\beta \in]0, \frac{\pi}{2}]$ refers to the angle of inclination formed between the wall and the horizontal direction. The Cartesian coordinate axes $\tilde{x}$ and $\tilde{y}$ are placed along the streamwise and crosswise flow directions, respectively, being the origin of the spatial reference frame located at the wall; $\tilde{t} \in \mathbb{R}_0^+$ specifies the time coordinate. Assume that, with the exception of density $\tilde{\rho} \in \mathbb{R}^+$, the physical properties of the liquid, such as dynamic viscosity $\tilde{\mu}_0 \in \mathbb{R}^+$ and surface tension $\tilde{\gamma}_0 \in \mathbb{R}^+$, are uniform within the physical fluid domain $\tilde{\Psi}$, defined as

$$\tilde{\Psi}(\tilde{t}) = \left\{ (\tilde{x}, \tilde{y}) \in \tilde{\mathbb{R}}^2 \mid 0 \leq \tilde{y} \leq \tilde{h}(\tilde{x}, \tilde{t}) \right\}, \tag{1}$$

where $\tilde{h}$ is a dimensional function tracing the spatial and temporal evolution of the wavy film free surface.

2.1. Governing equations

At the continuum level, the dimensional form of the governing equations of motion enforcing the conservation of mass and momentum for the compressible flow of the Newtonian falling film reads:

$$\partial_{\tilde{t}}\,\tilde{\rho} + \tilde{\nabla}\cdot(\tilde{\rho}\,\tilde{\mathbf{v}}) = 0 \tag{2a}$$

$$\tilde{\rho}\left(\partial_{\tilde{t}}\,\tilde{\mathbf{v}} + \left(\tilde{\mathbf{v}}\cdot\tilde{\nabla}\right)\tilde{\mathbf{v}}\right) = -\tilde{\nabla}\tilde{p} + \tilde{\rho}\,\boldsymbol{g} + \tilde{\mu}_0\left(\tilde{\nabla}^2\tilde{\mathbf{v}} + \left(\frac{1}{3}+\vartheta\right)\tilde{\nabla}(\tilde{\nabla}\cdot\tilde{\mathbf{v}})\right), \tag{2b}$$

where $\tilde{\mathbf{v}} = (\tilde{u},\, \tilde{v})$ and $\tilde{p}$ denote, respectively, the film velocity vector and the thermodynamic pressure, whereas $\boldsymbol{g} = (g\,\sin\beta,\, -g\,\cos\beta)$ is the gravitational acceleration. The parameter labelled by $\vartheta = \tilde{\zeta}_0/\tilde{\mu}_0$ expresses the ratio between the expansion viscosity $\tilde{\zeta}_0 \in \mathbb{R}$ and the dynamic viscosity $\tilde{\mu}_0$. Although ϑ is conventionally set to zero invoking Stokes' hypothesis ($\tilde{\zeta}_0 \equiv 0$) (Batchelor, 2000), we will not assume any particular value in order to preserve the widest possible generality throughout the paper. As will be demonstrated in § 3.2, this choice has no consequences in the ultimate formulation of the reduced model (25).

The flow system is subject to the following boundary conditions. At the rigid bottom $\tilde{y} = 0$, the no–slip and no–penetration conditions lead to

$$\tilde{\mathbf{v}}\big|_0 = \mathbf{0}. \tag{3}$$

At the free surface $\tilde{y} = \tilde{h}(\tilde{x}, \tilde{t})$, the balance of normal and tangential stress components for the shear–free film yields the dynamic coupling conditions

$$\left[\tilde{\mathbf{n}}^T\cdot\tilde{\mathbf{T}}^{(\tilde{\mathbf{n}})}\right] = \tilde{\gamma}_0\,\tilde{\nabla}\cdot\tilde{\mathbf{n}} \tag{4a}$$

$$\left[\tilde{\mathbf{t}}^T\cdot\tilde{\mathbf{T}}^{(\tilde{\mathbf{n}})}\right] = 0, \tag{4b}$$

where $\tilde{\gamma}_0$ is the surface tension and $\tilde{\mathbf{T}}^{(\tilde{\mathbf{n}})}$ is the fluid stress vector at the interface, whose orientation is determined by

$$\tilde{\mathbf{n}} = \left\{-\partial_{\tilde{x}}\tilde{h},\, 1\right\}^T \bigg/ \sqrt{1 + \left(\partial_{\tilde{x}}\tilde{h}\right)^2} \tag{5a}$$

$$\tilde{\mathbf{t}} = \left\{1,\, \partial_{\tilde{x}}\tilde{h}\right\}^T \bigg/ \sqrt{1 + \left(\partial_{\tilde{x}}\tilde{h}\right)^2} \tag{5b}$$

as normal and tangential unit column vector, respectively. Square brackets are used in (4) to designate the jump in any quantity of interest across the interface. Lastly, being the substantial derivative symbolised by $D(\star)/D\,\tilde{t} = \partial_{\tilde{t}}(\star) + \tilde{\mathbf{v}}\cdot(\tilde{\nabla}\star)$, an additional kinematic condition for the gas–liquid interface is introduced as follows

$$\frac{D}{D\,\tilde{t}}\left(\tilde{y} - \tilde{h}\left(\tilde{x},\, \tilde{t}\right)\right) = 0. \tag{6}$$

2.2. Scaling and dimensionless formulation

To make the problem dimensionless, we choose the value of the density at the gas–fluid interface as the reference scale for density $\tilde{\rho}_0$ in line with Richard (2021). This scale is convenient since at $\tilde{y} = \tilde{h}$ the hydrostatic contribution on pressure and density fields is depth–independent. The Nusselt film thickness $\tilde{h}_N$ (Nusselt, 1916) is chosen as the relevant length scale (figure 1), while we adopt the longitudinal characteristic speed as scale for the velocity $\tilde{U}_N = \tilde{q}_N/\tilde{h}_N = \tilde{\rho}_0\, g\, \sin\beta\, \tilde{h}_N^2\, /\, 3\, \tilde{\mu}_0$, where $\tilde{q}_N$ is the flow rate per unit of channel length:

$$\tilde{q}_N = \int_0^{\tilde{h}_N} \tilde{u}_N(\tilde{y})\, d\tilde{y}, \tag{7}$$

being $\tilde{u}_N(\tilde{y})$ the well–known Nusselt parabolic velocity profile (Nusselt, 1916).

The average velocity $\tilde{U}_N$ is indeed defined from the balance of the viscous friction force, $\propto \tilde{\mu}_0\, \tilde{U}_N\, /\, \tilde{h}_N^2$, and the streamwise gravity force, $\propto \tilde{\rho}_0\, g\, \sin\beta$.

The time and pressure scales are chosen as $\tilde{h}_N/\tilde{U}_N$ and $\tilde{\rho}_0\,\tilde{U}_N^2$, respectively (Lavalle et al., 2015).

As a customary practice in the study of the wavy film dynamics, we will adopt a shallow water approximation. Denoting by $\tilde{\mathcal{L}}$ a typical lengthwise distance characterizing superficial corrugations, we define the following film aspect ratio

$$\varepsilon = \frac{\tilde{h}_N}{\tilde{\mathcal{L}}} \ll 1, \tag{8}$$

as the scale parameter of the problem. Specifically, $\varepsilon \sim \partial_{x,\,t}\,(\star)$ accounts for the slowly–varying downstream modulations of the free surface with respect to space and time.

Thus, the governing equations (2) are rewritten in dimensionless terms:

$$\begin{aligned}
\partial_t\rho + \partial_x\left(\rho u\right) + \partial_y\left(\rho v\right) &= 0 && \text{(9a)}\\
\rho\,\varepsilon\left(\partial_t u + u\partial_x u + v\partial_y u\right) &= -\varepsilon\,\partial_x p + \frac{\rho}{Fr}\sin\beta + && \text{(9b)}\\
&+ \frac{1}{Re}\left[\partial_{yy}u + \varepsilon^2\partial_{xx}u + \varepsilon^2\left(\frac{1}{3}+\vartheta\right)\partial_x\left(\partial_x u + \partial_y v\right)\right] &&\\
\rho\,\varepsilon^2\left(\partial_t v + u\partial_x v + v\partial_y v\right) &= -\partial_y p - \frac{\rho}{Fr}\cos\beta + && \text{(9c)}\\
&+ \frac{\varepsilon}{Re}\left[\varepsilon^2\partial_{xx}v + \partial_{yy}v + \left(\frac{1}{3}+\vartheta\right)\partial_y\left(\partial_x u + \partial_y v\right)\right], &&
\end{aligned}$$

being $Re = \tilde{\rho}_0\,\tilde{U}_N\,\tilde{h}_N/\tilde{\mu}_0$ and $Fr = \tilde{U}_N^2/g\,\tilde{h}_N$ the Reynolds number and the Froude number, respectively, with $(x, y, t) \in \mathbb{R} \times [0, h] \times [0, +\infty[$.

The system (9) is coupled with the following set of dimensionless boundary conditions:

$$u\big|_0 = v\big|_0 = 0 \tag{10a}$$

$$Re\left(1+\varepsilon^2\partial_x^2 h\right)\left(p\big|_h - p_i\right) + \varepsilon\left(\frac{2}{3}-\vartheta\right)\left(1+\varepsilon^2\partial_x^2 h\right)\left(\partial_x u\big|_h + \partial_y v\big|_h\right) + \tag{10b}$$

$$-2\,\varepsilon\left(\partial_y v\big|_h + \varepsilon^2\partial_x^2 h\,\partial_x u\big|_h\right) + 2\,\varepsilon\,\partial_x h\left(\partial_y u\big|_h + \varepsilon^2\partial_x v\big|_h\right) = -\frac{Re}{We}\frac{\varepsilon^2\partial_{xx}h}{\sqrt{1+\varepsilon^2\partial_x^2 h}}$$

$$2\,\varepsilon^2\partial_x h\left(\partial_y v\big|_h - \partial_x u\big|_h\right) + \left(1-\varepsilon^2\partial_x^2 h\right)\left(\partial_y u\big|_h + \varepsilon^2\partial_x v\big|_h\right) = 0 \tag{10c}$$

$$\partial_t h + u\big|_h\,\partial_x h = v\big|_h\,, \tag{10d}$$

where p_i is the dimensionless atmospheric pressure exerted at the film interface and $We = \tilde{\rho}_0\,\tilde{h}_N\,\tilde{U}_N^2/\tilde{\gamma}_0$ is the Weber number.

3. Low–dimensional modelling

Here, the free–surface flow problem is tackled adopting an asymptotic approximation of the continuity and the Navier-Stokes equations based on the film aspect ratio $\varepsilon \ll 1$ introduced in § 2.2. A great simplification can be accomplished by means of a boundary layer approach together with a depth–averaging technique. Such a procedure leads to the determination of a reduced coupled system of two equations, having the film thickness $h\,(x,t)$ and the flow rate per unit of channel width $q\,(x,t)$ as local dimensionless unknowns. We propose a two–equation momentum–integral model (MIM) that is accurate up to and including order $O(\varepsilon^2)$ both in inertial and in viscous diffusion terms. Based on this approximation, the problem expressed by (9, 10) will be consistently simplified accounting for the higher magnitude of surface tension, $We = O(\varepsilon^2)$, compared to inertia–related phenomena, $Re \sim Fr = O(1)$.

Following the classical Polhausen–von Kármán momentum–integral analysis, the y–momentum equation (9c) and related boundary condition (10b) serve to eliminate the streamwise pressure gradient term $\partial_x p$ in the x–momentum equation (9b). Being this term of $O(\varepsilon)$, it is sufficient to retain (9c) and (10b) up to $O(\varepsilon)$. Differently from the incompressible scenario, in this work, a supplementary constitutive relation is required to describe completely the fluid system due to the presence of a density term $\rho = \tilde{\rho}/\tilde{\rho}_0 = O(1)$ as an additional unknown (Richard, 2021).

3.1. Barotropic equation of state

Since it is difficult to encounter large variations in density in gravity–driven falling films, we make use of the following linearised Equation of State (EoS)

$$\tilde{\rho}\left(\tilde{p}, \tilde{T}, \tilde{S}\right) = \tilde{\rho}|_{\tilde{h}} + \left(\frac{\partial \tilde{\rho}}{\partial \tilde{p}}\right)_{\tilde{T},\tilde{S}} (\tilde{p} - \tilde{p}|_{\tilde{h}}) + \left(\frac{\partial \tilde{\rho}}{\partial \tilde{T}}\right)_{\tilde{p},\tilde{S}} \left(\tilde{T} - \tilde{T}|_{\tilde{h}}\right) + \left(\frac{\partial \tilde{\rho}}{\partial \tilde{S}}\right)_{\tilde{p},\tilde{T}} \left(\tilde{S} - \tilde{S}|_{\tilde{h}}\right), \tag{11}$$

in the form of a first–order truncated Taylor series expansion as in Batchelor (2000); Colinet et al. (2001). The validity of (11) is intended to be restricted to a neighborhood of the reference state, *i.e.* $\tilde{\rho} - \tilde{\rho}|_{\tilde{h}} \ll 1$. Specifically, besides pressure $\tilde{p}$, the parameters that characterize such a functional dependence are the fluid temperature $\tilde{T}$ and its entropy $\tilde{S}$ for a fixed vector of amounts of constituents.

At the present stage, density–affecting thermal effects – which would have required an energy equation coupling – will be ignored, so as to confine our current inquiry to a two–equation MIM pattern. Moreover, although the flow is not itself homentropic, the propagation of small–amplitude long–wave perturbations is shown to be scarcely affected by acoustic attenuation and dispersion phenomena (Van Dael, 1968; Kinsler et al., 2000). We postpone a more rigorous proof of this statement to § 6.1, where we deal with the notion of wave hierarchy.

Therefore, the EoS (11) is reduced to a *barotropic* formulation where density variations with pressure support the propagation of sound waves:

$$\tilde{\rho}\left(\tilde{p}\right) = \tilde{\rho}_0 + \left(\frac{\partial \tilde{\rho}}{\partial \tilde{p}}\right)_{\tilde{S}} \left(\tilde{p} - \tilde{p}|_{\tilde{h}}\right). \tag{12}$$

Notably, one can refer to the thermodynamic definition of isentropic speed of sound (Shapiro, 1953)

$$\tilde{a}_0 = \sqrt{\left(\frac{\partial \tilde{p}}{\partial \tilde{\rho}}\right)_{\tilde{S}}}, \tag{13}$$

whose magnitude $\tilde{a}_0$ is supposed to be uniform and constant within $\tilde{\Psi}$, in order to achieve the dimensionless version of (11), which ultimately reads

$$\rho\left(p\right) = 1 + Ma^2 \left(p - p|_h\right). \tag{14}$$

In (14) an overall Sarrau–Mach number

$$Ma = \frac{\tilde{U}_N}{\tilde{a}_0} \in \mathbb{R}^+, \tag{15}$$

expressing the magnitude of inertial forces with respect to elastic ones, has been introduced as dimensionless group to capture the influence of compressibility on the film flow. As it can be inferred from (14), the classical incompressible limit is recovered as a limiting case when the acoustic propagation is modelled as an instantaneous phenomenon, *i.e.* $\tilde{a}_0 \to +\infty \Longleftrightarrow Ma \to 0^+$.

3.1.1. Pressure distribution

Replacement of (14) into the $O(\varepsilon)$ estimate of (9c) leads to the following first—order linear non–homogeneous Ordinary Differential Equation (ODE) with respect to the crosswise coordinate y for the film pressure $p\,(x, y, t)$:

$$\partial_y p + \frac{\cos\beta}{Fr} Ma^2\, p = \frac{\cos\beta}{Fr}\left(Ma^2\ p|_h - 1\right) + \frac{\varepsilon}{Re}\,\partial_y \mathcal{W} + O(\varepsilon^2), \tag{16}$$

in which the function $\mathcal{W}(u,\, v;\, \vartheta) = \partial_y v + \left(\frac{1}{3} + \vartheta\right)(\partial_x u + \partial_y v)$ implicitly depends on y through the dimensionless velocity field. The solution of (16), in which the dimensionless interfacial pressure $p|_h$ has been evaluated using the normal stress boundary condition (10b), is determined as summation of the particular solution of (16) and the solution of the corresponding homogeneous ODE. The latter is obtained via the method of separation of variables, whereas the former through the technique of variation of parameters (sometimes referred to as Duhamel's principle). As a result, the proper solution of (16) reads:

$$\begin{aligned} p(x, y, t; \vartheta) \;&=\; p_i + \frac{\overbrace{\exp\left[\dfrac{\cos\beta}{Fr} Ma^2\,(h-y)\right]}^{\blacklozenge} - 1}{Ma^2} - \frac{\varepsilon^2}{We}\partial_{xx} h + \\ &+\; \frac{\varepsilon}{Re}\Big(\mathcal{W} - (\partial_x u)|_h\Big) + O(\underbrace{\varepsilon\, Ma^2}_{\clubsuit}), \end{aligned} \tag{17}$$

being its full–form given in Appendix A. As expected, as the Mach number approaches zero, (17) reduces to the pressure distribution obtained by Ruyer-Quil and Manneville (1998) in the context of a perfectly incompressible free–surface flow, by virtue of the exponential limit $(e^{m\star} - 1)/\star \to m$ for vanishing $\star$ (with $m \in \mathbb{R}\backslash\{0\}$), along with the incompressible continuity identity $\partial_y v = -\partial_x u$.

Based on the above considerations, the barotropic EoS (14) can be recast as

$$\rho\,(x,y,t;\vartheta) = \underbrace{\exp\left[\frac{\cos\beta}{Fr} Ma^2\,(h-y)\right]}_{\blacklozenge} + O(\underbrace{\varepsilon\,Ma^2}_{\clubsuit}). \tag{18}$$

3.1.2. Weak compressibility hypothesis

Although the flow compressibility is taken into account in this model, thin descending liquid films usually show a weakly compressible behaviour and, therefore, the expression (18) can be simplified. To do so, the magnitude of the Mach number can be estimated with respect to ε and, taking inspiration from Richard (2021), we can write

$$Ma = M\,\varepsilon^{\alpha}, \tag{19}$$

where α controls the compressibility behaviour and $M = O(1) \in \mathbb{R}_0^+$. As a consequence, the accuracy of the model is retained only if $\alpha \geq 1$ since the residual term $\clubsuit$ in (18) is of $O(2\alpha+1)$. In our model, the Mach number enters into the governing equations only through the barotropic EoS (14) and, since $Ma^2 = O(\varepsilon^{2\alpha})$, the different orders in terms of integer power of the Mach number can be classified as $\alpha = \{1,\, 3/2,\, 2,\, 5/2,\, \ldots\}$.

An estimation of the order of magnitude of the exponential term $\blacklozenge$ in (17, 18) within the low–Ma limit requires one to take the Maclaurin series expansion $e^{\star} = \sum_{n=0}^{\infty} (\star^n/n!)$, that, together with the preliminary guess about the order of magnitude of $Fr = O(1)$, yields to:

$$\underbrace{\exp\left[\frac{\cos\beta}{Fr} Ma^2\,(h-y)\right]}_{\blacklozenge} \approx 1 + \underbrace{\frac{\cos\beta}{Fr} Ma^2\,(h-y)}_{\blacklozenge_1} + \frac{1}{2}\underbrace{\left[\frac{\cos\beta}{Fr} Ma^2\,(h-y)\right]^2}_{\blacklozenge_2}, \tag{20}$$

implying that $\blacklozenge_1 = O(\varepsilon^{2\alpha})$ and $\blacklozenge_2 = O(\varepsilon^{4\alpha})$. Depending on the value of α, a twofold level of compressibility can be consequently addressed in view of the prescribed $O(\varepsilon^2)$ accuracy criterion:

$$\rho\,(x,y,t;\vartheta) = \begin{cases} 1 + O(\varepsilon^3), & \alpha \geq \frac{3}{2} \\ 1 + \frac{\cos\beta}{Fr} Ma^2\,(h-y) + O(\varepsilon^3), & \alpha = 1. \end{cases} \tag{21}$$

Thus, when $\alpha \geq 3/2$ the analysis is formally identical to the incompressible scenario, since a relation of asymptotic equivalence holds between $\tilde{\rho}\,(x,y,t)$ and $\tilde{\rho}_0$. In other words, the relation (19) provides a rule–of–thumb criterion for the film flow to be considered as weakly–compressible in asymptotic terms. For example, if we assume $\varepsilon = 0.01$ as long–wave parameter (jointly with a unitary–valued M), we find the threshold for incompressibility as $Ma \lesssim 0.001$.

3.2. Boundary layer equations

In this this paper we focus on the weakly–compressible regime corresponding to $\alpha = 1$. In this scenario, the derivative of the pressure distribution (17) is computed using the expression (21) with $\alpha = 1$, leading to

$$\begin{aligned} \partial_x p\,(x,y,t;\vartheta) = \frac{\cos\beta}{Fr}\partial_x h - \frac{\varepsilon^2}{We}\partial_{xxx} h + \\ + \frac{\varepsilon}{Re}\left[\partial_{xy} v + \left(\frac{1}{3} + \vartheta\right)\partial_x\left(\partial_x u + \partial_y v\right) - \partial_x\left((\partial_x u)|_h\right)\right] + O(\varepsilon^2). \end{aligned} \tag{22}$$

As mentioned above, (22) is now substituted in lieu of $\partial_x p$ in (9b), showing that ϑ–dependent contributions mutually cancel themselves out.

Then, the replacement of ρ and $\partial_x p$ jointly permits obtaining the second–order set of weakly compressible Boundary Layer Equations (BLEs), which finally reads:

$$\partial_x u + \partial_y v + \tfrac{\cos\beta}{Fr}\, Ma^2\, \left(\partial_t h + u\partial_x h - v\right) = 0 \tag{23a}$$

$$\varepsilon\, \left(\partial_t u + u\partial_x u + v\partial_y u\right) = \tfrac{\partial_{yy} u}{Re} + \tfrac{\varepsilon^3}{We}\partial_{xxx} h - \varepsilon\, \tfrac{\cos\beta}{Fr}\partial_x h + \tag{23b}$$
$$+ \tfrac{\sin\beta}{Fr}\left(1 + \tfrac{\cos\beta}{Fr} Ma^2\, (h-y)\right) + \tfrac{\varepsilon^2}{Re}\Big[\partial_{xx} u - \partial_{xy} v + \partial_x\left((\partial_x u)|_h\right)\Big].$$

By resorting to Leibniz's integral rule, BLEs (23) are integrated over the depth $\int_0^h (\star)\, dy$ to reduce the space dimensionality of the problem. The basic idea behind this modelling strategy is the elimination of the cross-stream flow dependency (Ruyer-Quil and Manneville, 2000).

Unfortunately, the resulting BLEs fail to be entirely expressed in terms of the local film thickness $h\,(x,\, t)$ and the local flow rate $q\,(x,\, t) = \int_0^h u(y)\, dy$. Thus, closure laws are needed in (23b) for the following terms: the so–called shape factor $\int_0^h u^2\, dy$, the difference between interfacial and wall shear stresses $((\partial_y u)|_h - (\partial_y u)|_0)$, and the antiderivative of other second–order terms within square brackets ($\propto \varepsilon^2/Re$). Moreover, since the compressibility introduces a novel second–order contribution, related to the crosswise component of velocity, *viz.* $\int_0^h v\, dy$, in (23a) an additional closure is required. Such closures can be obtained via the explicit expression for the unknown velocity field $u\,(x, y, t)\,,\; v\,(x, y, t)$.

3.2.1. Long–wave approximation

In this work, we adopt a long wave approach following the classical Benney's closure technique (Benney, 1966; Gjevik, 1970; Lin, 1974; Chang, 1986). Accordingly, each variable $\mathcal{V} = \{u,\, v,\, p,\, \rho\}$ appearing in the primitive problem is decomposed as a formal power–series regular perturbation expansion, having ε as basis:

$$\mathcal{V}^{(\varepsilon)} = \mathcal{V}^{(0)} + \varepsilon\, \mathcal{V}^{(1)} + \varepsilon^2\, \mathcal{V}^{(2)} + \ldots \,. \tag{24}$$

The right–hand side of (24) is ideal for assessing the effect of a small perturbation in ε about zero, provided that proper accuracy constraints are met (Simmonds and Mann Jr, 1998). Specifically, mathematical convergence of the infinite series (24) is not necessary (Jeffreys, 1926; Van Dyke and Rosenblat, 1975). On the other hand, it is required that – once truncated – $\mathcal{V}^{(\varepsilon)}$ rapidly approaches $\mathcal{V}$ in the limit of vanishing ε. This is equivalent to enforce that the approximation error $\left|\mathcal{V} - \mathcal{V}^{(\varepsilon)}\right|$ scales as the first neglected term of the series (24). By assuming this residue to be $\sim \varepsilon^3$, the $O(\varepsilon^2)$ truncation of the previous ansatz (24) can be then substituted in (9, 10, 14), allowing the corresponding equations to be broken up into different orders and sequentially solved. Specifically, the $O(\varepsilon^0,\ \varepsilon^1)$ restrictions of the problem coincide with their respective incompressible versions, due to the fact that *Ma*–related influence intervenes only at $O(\varepsilon^2)$ when $\alpha = 1$, through the equality $\rho^{(2)} = M^2 \left(p^{(0)} - p^{(0)}\big|_h\right)$ by (14). Also, the terms including the expansion viscosity appear to be irrelevant, due to the fact that the $O(\varepsilon^0,\ \varepsilon^1)$ velocity fields are solenoidal. Hence, a comparison between the compressible second–order profiles and their incompressible analogues will be helpful to understand the impact of a varying density on flow–related quantities; this aspect will be discussed in § 6.2.

3.3. Depth–averaged model

Upon substitution, we now take advantage of the expressions for the asymptotic expansions determined beforehand. These are confined to Appendix B only for the sake of brevity.

In order to derive the depth–integral model, three steps need to be performed: (i) replace higher–order time derivatives of h by virtue of a consistent estimate of the kinematic boundary condition (10d), (ii) replace space derivatives of q – except for the diffusive term $\partial_{xx}q$ – by the corresponding consistent asymptotic expansions, and (iii) add to the r.h.s. of (23b) the higher–order residue $+3\left(q^{(0)}+\varepsilon q^{(1)}+\varepsilon^2 q^{(2)}-q\right)/\,Re\,h^2 = O(\varepsilon^3)$, so to preclude algebraic cancellation of linear source terms – see (26) – as part of the model quasi–linear reformulation (Lavalle et al., 2015). After these manipulations, the following depth–averaged closed set of two evolution equations is obtained:

$$\partial_t h + \partial_x q - \frac{\Lambda\cos\beta\, h^3\,(\partial_x h)}{2\,Fr}\,Ma^2 = 0 \tag{25a}$$

$$\begin{aligned}
&\frac{h\,(\partial_x h)\cos\beta\,\varepsilon}{Fr} + \frac{3\,h^4\,(\partial_x h)\,\Lambda^2\,\varepsilon}{5} + \varepsilon\,(\partial_t q) = \frac{h\,(\partial_{xxx}h)\,\varepsilon^3}{We} + \\
&\quad -\frac{4\,Re\,h^5\,(\partial_{xxxx}h)\,\Lambda\,\varepsilon^4}{21\,We} - \frac{2\,Re\,h^4\,(\partial_x h)\,(\partial_{xxx}h)\,\Lambda\,\varepsilon^4}{3\,We} + \\
&\quad +\frac{2\,Re\,h^4\,(\partial_{xx}h)^2\,\Lambda\,\varepsilon^4}{5\,We} + \frac{4\,Re\,h^3\,(\partial_x h)^2\,(\partial_{xx}h)\,\Lambda\,\varepsilon^4}{5\,We} + \\
&\quad +\frac{4\,Re\,h^5\,(\partial_{xx}h)\,\Lambda\cos\beta\,\varepsilon^2}{21\,Fr} + \frac{16\,Re\,h^4\,(\partial_x h)^2\,\Lambda\,\cos\beta\,\varepsilon^2}{15\,Fr} + \\
&\quad +\frac{3\,Ma^2\,h^2\,\Lambda\,\cos\beta}{8\,Fr\,Re} - \frac{8\,Re\,h^8\,(\partial_{xx}h)\,\Lambda^3\,\varepsilon^2}{105} - \frac{23\,Re\,h^7\,(\partial_x h)^2\,\Lambda^3\,\varepsilon^2}{35} + \\
&\quad +\frac{h^2\,(\partial_{xx}h)\,\Lambda\,\varepsilon^2}{Re} + \frac{3\,h\,(\partial_x h)^2\,\Lambda\,\varepsilon^2}{Re} + \frac{2\,(\partial_{xx}q)\,\varepsilon^2}{Re} + \frac{h\,\Lambda}{Re} - \frac{3\,q}{Re\,h^2},
\end{aligned} \tag{25b}$$

where the dimensionless number Λ is defined as $Re/Fr\,\sin\beta$. Here, by using the definitions of $\tilde{U}_N$, Re and Fr, we get that $\Lambda = 3$. In other contexts, this parameter may assume different values, such as when a different characteristic speed is used instead of Nusselt integral velocity $\tilde{U}_N$, in case of a fluid exhibiting a non–Newtonian constitutive behaviour (Noble and Vila, 2013), or in presence of a variable or uneven interfacial pressure p_i; it has been decided not to replace Λ by any numerical value (Richard et al., 2019) only to prevent loss of generality.

With reference to equation (25b), it is worth pointing out two additional facts. (i) Higher–order and non–linear capillary terms have been explicitly and fully retained, unlike what customarily developed (Ruyer-Quil and Manneville, 1998; Richard et al., 2016, 2019). In fact, their contribution could be equally gathered on the l.h.s. within the canonical convective term proportional to $\varepsilon\,\partial_x\,(q^2/h)$, leading to an equivalent model in terms of consistency. (ii) Inertial terms have been maintained up to $O(\varepsilon^2)$, dissimilarly from the well–established practice of relying on a simplified model (Ruyer-Quil and Manneville, 2002). In fact, we are interested in comparing the whole second–order expansions with their incompressible analogues.

The derived shallow–water system (25) constitutes a second–order reduced model describing the weakly–compressible free–surface flow of a wavy gravity–driven Newtonian falling film. In the scenario where the temperature field within the liquid film yields density variations, the EoS (12) should be modified accordingly to take into account density–affecting thermal effects. In addition, the model (25) should be coupled to an integral form of the energy equation to characterise the interplay between hydrodynamics, compressibility and heat transfer. For this, reduced models for non–isothermal (incompressible) falling films have been successful in solving the heat transfer across the liquid film (Trevelyan et al., 2007; Thompson et al., 2019; Cellier and Ruyer-Quil, 2020).

4. Temporal linear stability

A temporal stability analysis relies on the existence of a steady solution about which perturbations are superimposed. Let $\mathbf{Q}(x,\,t) = \{h(x,t),\, q(x,t)\}^T$ represent the column vector containing the two unknown integral variables describing the film descent. Indeed, the weakly–compressible shallow–water equations (25) possibly admit to be recast as

$$\partial_t\,\mathbf{Q} + \partial_x\,\mathcal{F}(\mathbf{Q}) = \mathcal{S}(\mathbf{Q})\,, \tag{26}$$

where $\mathcal{F}$ is the associated flux vector whereas $\mathcal{S}$ gathers source terms together (Noble and Vila, 2014).

4.1. Normal mode analysis

The linear stability problem of the low–dimensional weakly–compressible model (25) is approached through normal mode decomposition, according to which a harmonic infinitesimal disturbance $\mathbf{Q}_p$, having $\|\hat{\mathbf{Q}}\| \ll 1$ as amplitude, is added to the Nusselt base state. The latter is explained in terms of the dimensionless uniform parallel solution $\mathbf{Q}_0 = \{h_0,\, q_0\}^T$, in which $h_0 = \tilde{h}_0/\tilde{h}_N \equiv 1$ by definition, whereas the novel expression for the compressible primary discharge q_0 will be disclosed as part of the linearisation process. Accordingly, it is written

$$\mathbf{Q}(x,t) = \mathbf{Q}_0 + \mathbf{Q}_p(x,t) \tag{27a}$$

$$\mathbf{Q}_p(x,t) = \hat{\mathbf{Q}}\,\exp\left[\,i\,k\,(x - c\,t)\right], \tag{27b}$$

where it remains understood that $k = 2\pi\,\tilde{h}_N/\tilde{\mathcal{L}} \in \mathbb{R}^+$ and $c = c_r + i\,c_i \in \mathbb{C}$ are, respectively, the dimensionless real wave–number and the complex wave celerity of the propagating sine–type pulse. In particular, c_r accounts for its phase velocity, whereas $k\, c_i$ determines its degree of amplification or damping, depending on its sign: with reference to (27b), instability of the mean flow evidently sets in on the condition that $k\, c_i > 0$.

4.1.1. Base flow calculation

Quasi–linear conservation form (26) actually stipulates a formal relation between differential operators (Meliga et al., 2010) in such a way that

$$\mathcal{S}(\mathbf{Q}_0) = 0 \tag{28}$$

restores the equilibrium condition constraining the dimensionless compressible base flow rate $q_0\,(Re,\,\beta,\,Ma)$ to the dimensionless waveless thickness h_0. Solving (28) we find:

$$q_0 = \frac{\Lambda\, h_0^3}{3} \left(1 + \overbrace{\frac{3}{8}\, \frac{Ma^2\, \Lambda\, \cot\beta\, h_0}{Re}}^{\Delta\, q_{0,\,\mathrm{rel}}^{(2)}} \right), \tag{29}$$

which explicitly shows that compressibility entails a relative increase in the equilibrium flow rate q_0, according to the over–bracketed second–order contribution denoted as $\Delta\, q_{0,\,\mathrm{rel}}^{(2)}$, with respect to its incompressible limit $q_0^{Ma\to 0^+} = \Lambda\, h_0^3/3$. Expression (29) likewise coincides with the stationary waveless solution associated to system (23) in the case of unidirectional flow. Compressible effects are kept at the base flow level $\mathbf{Q}_0$, on which linear disturbances $\mathbf{Q}_p$ develop, by means of a small additive contribution to the incompressible ground–state flow rate $q_0^{Ma\to 0^+}$. Such a correction $(q_0^{Ma\to 0^+}\, \Delta\, q_{0,\,\mathrm{rel}}^{(2)})$ appears to be of $O(\varepsilon^2)$ since, choosing $\alpha = 1$, we assumed Ma to be of order $O(\varepsilon)$.

4.1.2. Model dispersion relation

Dropping higher–order perturbations and plugging (27) into (25) yields the following matrix–form differential system:

$$\begin{aligned}
&\partial_t \mathbf{Q}_p + \begin{bmatrix} a_{11} & 1 \\ a_{21} & 0 \end{bmatrix} \partial_x \mathbf{Q}_p = \begin{bmatrix} 0 & 0 \\ b_{21} & b_{22} \end{bmatrix} \mathbf{Q}_p + \\
&+ \begin{bmatrix} 0 & 0 \\ c_{21} & c_{22} \end{bmatrix} \partial_{xx} \mathbf{Q}_p + \begin{bmatrix} 0 & 0 \\ s_{21} & 0 \end{bmatrix} \partial_{xxx} \mathbf{Q}_p + \begin{bmatrix} 0 & 0 \\ d_{21} & 0 \end{bmatrix} \partial_{xxxx} \mathbf{Q}_p,
\end{aligned} \tag{30}$$

where

$$a_{11} = -\frac{Ma^2\, h_0^3\, \Lambda^2\, \cot\beta}{2\, Re} \qquad b_{21} = \frac{3\,\Lambda}{Re} + \frac{3}{2}\frac{Ma^2\, h_0\, \Lambda^2\, \cot\beta}{Re^2} \tag{31a}$$

$$a_{21} = \frac{3}{5}\, h_0^4\, \Lambda^2 + \frac{h_0\, \Lambda\, \cot\beta}{Re} \qquad b_{22} = -\frac{3}{Re\, h_0^2} \qquad c_{22} = \frac{2}{Re} \qquad s_{21} = \frac{h_0}{We} \tag{31b}$$

$$c_{21} = \frac{4}{21} h_0^5\, \Lambda^2\, \cot\beta - \frac{8}{105}\, Re\, h_0^8\, \Lambda^3 + \frac{h_0^2\, \Lambda}{Re} \qquad d_{21} = -\frac{4}{21}\frac{Re\, h_0^5\, \Lambda}{We}. \tag{31c}$$

Expressions (31b – 31c) do not incorporate the Mach number, thus ε has been legitimately replaced there by a unitary value (Richard et al., 2019). Such assignment is based on the fact that pertinent orders of magnitude have been already accounted for in the integral model (25).

Equation (30) accounts for the normal mode evolution (27b) under the form of a generalised algebraic eigenvalue problem for c and $\hat{\mathbf{Q}}$, having $\langle k;\ Re,\ \beta,\ We,\ Ma\rangle$ as independent set of relevant parameters. Seeking a non–trivial solution, one has to impose that the matrix associated to the linearised system is degenerate. This leads to a quadratic polynomial dispersion relation over the complex field in the phase speed c with complex k–dependent coefficients, written as

$$- k\, c^2 + \left[a_{11}\, k + i\, \left(b_{22} - k^2\, c_{22}\right)\right]\, c +$$
$$+\; k^3\, s_{21} + k\, a_{21} + i\, \left[d_{21}\, k^4 + \left(a_{11}\, c_{22} - c_{21}\right)\, k^2 + \left(b_{21} - a_{11}\, b_{22}\right)\right] = 0. \quad (32)$$

4.2. Celerity long–wave expansion

Following Yih (1963), we consider the temporal stability problem in terms of an asymptotic expansion of the wave celerity $c(k)$ into successive powers of the wavenumber k:

$$c = c^{(0)} + k\, c^{(1)} + k^2\, c^{(2)} + k^3\, c^{(3)} + \ldots, \quad (33)$$

within the limit provided by the long–wave approximation ($k \ll 1$) assumed in this work. In analogy with the closure algorithm illustrated in § 3.2.1, the expansion (33) is substituted into the dispersion relation (32). Ensuring that each order in k satisfies (32), we get a cascade of equations from which the higher–order celerities $c^{(n)}(k)$ ($n = 0, 1, 2, \ldots$) are obtained. Although evolution equations (25) are consistent up to $O(\varepsilon^2)$, we intentionally take the expansion (33) for the celerity $c(k)$ up to its successive order in terms of k, that is until $O(k^3)$. In this way, we can test the accuracy of the present model (25) in its incompressible limit $Ma \to 0^+$, by setting the benchmark against the Orr–Sommerfeld stability problem (Orr, 1907; Sommerfeld, 1908) at the corresponding order. Such a comparative approach constitutes a well–trodden path among the falling–film community (Ruyer-Quil and Manneville, 1998; Samanta et al., 2011; Samanta, 2014; Richard et al., 2016). Specifically, we obtain:

$$c^{(0)} = 3 \tag{34a}$$

$$c^{(1)} = 3\,i\left(\frac{2}{5}\,Re - \frac{1}{3}\,\cot\beta + \Gamma_2^{(1)}\,Ma^2\,\cot\beta\right) \tag{34b}$$

$$c^{(2)} = 3\left(-1 + \frac{10}{21}\,Re\,\cot\beta - \frac{4}{7}\,Re^2 + \Gamma_2^{(2)}\,Ma^2\,\cot\beta\, + \Gamma_4^{(2)}\,Ma^4\,\cot^2\beta\right) \tag{34c}$$

$$\begin{aligned} c^{(3)} = 3\,i\Bigg(& -\frac{1}{9}\,Re\,\cot^2\beta + \frac{128}{105}\,Re^2\,\cot\beta + \frac{2}{9}\,\cot\beta - \frac{Re}{9\,We} - \frac{228}{175}\,Re^3 + \\ & -\frac{34}{15}\,Re\, + \Gamma_2^{(3)}\,Ma^2\,\cot\beta\, + \Gamma_4^{(3)}\,Ma^4\,\cot^2\beta\, + \Gamma_6^{(3)}\,Ma^6\,\cot^3\beta\Bigg), \end{aligned} \tag{34d}$$

in which we use the equality $\Lambda = 3$ and the identity $h_0 \equiv 1$. Those expressions for the wave celerities have been written to highlight the effect of the compressibility. In fact, the expansions (34) are impacted by compressibility from $n = 1$ onwards ($n = 1, 2, \ldots$) through additive contributions that take the form $\Gamma_{2j}^{(n)}\,Ma^{2j}\,\cot^j\beta$, with $1 \leq j \leq n$. These are found to be:

$$\Gamma_2^{(1)} = \frac{3}{2} \qquad \Gamma_2^{(2)} = \frac{1}{2}\,\cot\beta - \frac{18}{5}\,Re - \frac{1}{Re} \tag{35a}$$

$$\Gamma_4^{(2)} = -\frac{9}{4} \qquad \Gamma_2^{(3)} = \frac{19}{7}\,Re\,\cot\beta - \frac{324}{35}Re^2 - \frac{9}{2} \tag{35b}$$

$$\Gamma_4^{(3)} = \frac{3}{4}\,\cot\beta - \frac{243}{20}\,Re - \frac{3}{2\,Re} \qquad \Gamma_6^{(3)} = -\frac{27}{8}. \tag{35c}$$

In accordance with the adopted standard of accuracy, the current model is consistent with the asymptotic expansions of solutions to Orr–Sommerfeld boundary–value problem, reported in Ruyer-Quil and Manneville (1998), in the limit of $Ma \to 0^+$: (25) is able to correctly recover $c^{(0)}$, $c^{(1)}\big|_{Ma\to 0^+}$ and $c^{(2)}\big|_{Ma\to 0^+}$, but it manifests disagreements on successive orders. For more in–depth reflection on such validation the reader is referred to Appendix C, being the primary focus of sections §§ 4, 5 upon the influence of a weak compressibility on the linear stability.

5. Results and discussion

In this section we examine the relations (34) in the light of the well–known results from Kapitza (1948) and Benjamin (1957). The $O(k^0)$ celerity (34a) immediately captures the classical phase speed of free–surface waves, which travel three times faster than the averaged flat film, regardless of its compressible behavior. Due to the nature of (14) as EoS, the compressibility terms controlled by the Mach number affect only even powers Ma^{2j} throughout $O(k^n)$ expansions (34b – 34d), for $1 \leq j \leq n$.

Secondly, as evidenced by the relations (34) and (31a), a vertical liquid film is not affected by the compressibility since $\cot\left(\frac{\pi}{2}\right) = 0$ in (25). On the other hand, when the plate is horizontal, $\beta = 0$ and no gravity–driven drainage is possible.

5.1. Impact of compressibility on the wave celerity

Differently from the incompressible Navier–Stokes equations, whose temporal stability analysis is pursued through numerical solution of the Orr–Sommerfeld fourth–order differential problem in the cross–stream coordinate, in this case the dispersion relation (32) is a quadratic polynomial equation in $c(k)$, which is easily solvable numerically.

Initially, we consider a falling liquid film whose incompressible flow is marginally stable. This case will be shown to be the most favourable to discern compressibility–related effects on the film flow stability within the investigated weakly–compressible regime. The plate is angled at $\beta = 4.6°$. As an aside, this choice enables us to compare the wave celerity and growth rate (see Appendix C) between the results presented here within the incom-

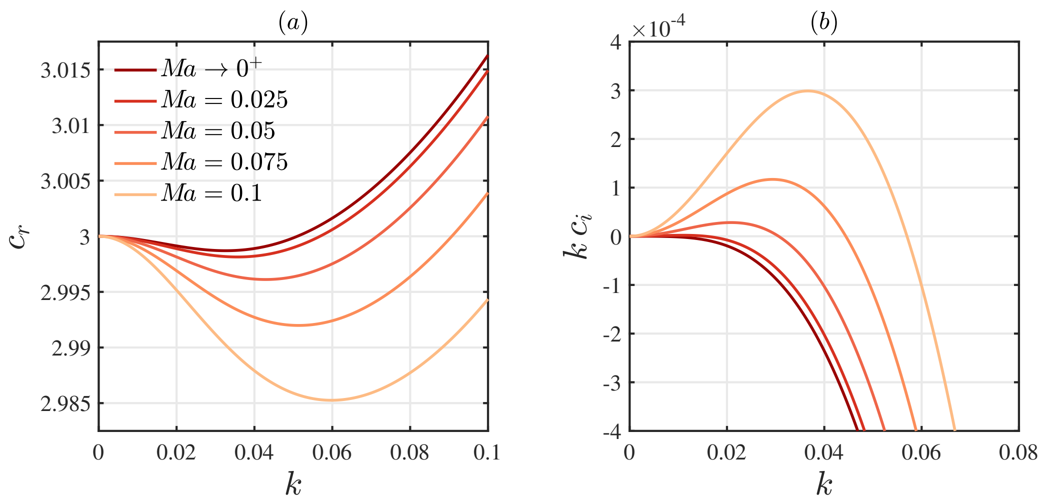

Figure 2: Impact of compressibility on the graphical representation of solutions to the dispersion relation (32) for the second–order integral model (25), in terms of (a) phase speed c_r and (b) growth rate $k\,c_i$ as a function of the dimensionless wavenumber k, for different small values of the Mach number Ma, displayed in the legend. The axes are dimensionless. The data used are taken from Brevdo et al. (1999) and correspond to the following set of values: $g = 9.81\,\mathrm{m\,s^{-2}}$, $\beta = 4.6°$, $Re = 5/6\,\cot\beta = 10.357$, $\tilde{\rho}_0 = 1130\,\mathrm{kg\,m^{-3}}$, $\tilde{\mu}_0 = 5.673\,10^{-3}\,\mathrm{Pa\,s}$, $\tilde{\gamma}_0 = 69.0\,10^{-3}\,\mathrm{N\,m^{-1}}$. Comparison with Brevdo et al. (1999) is shown in Appendix C for the incompressible scenario.

pressible limit $Ma \to 0^+$ (dark red line in figure 2) and those determined by Brevdo et al. (1999) for a perfectly incompressible falling film in a passive atmosphere. The effects of compressibility on the hydraulic branch solving (32) both in its real and imaginary parts are displayed in figure 2a, b respectively, for sufficiently small values of the Mach number $Ma = O(\varepsilon)$. Specifically, the evolution of the phase speed $c_r(k)$ bends downwards as the Mach number increases. Nonetheless, the same long–wave limit $c^{(0)}$ is recovered, as established by (34a). The delaying effect of compressibility on the phase velocity of linear waves (Richard et al., 2019) finds confirmation in

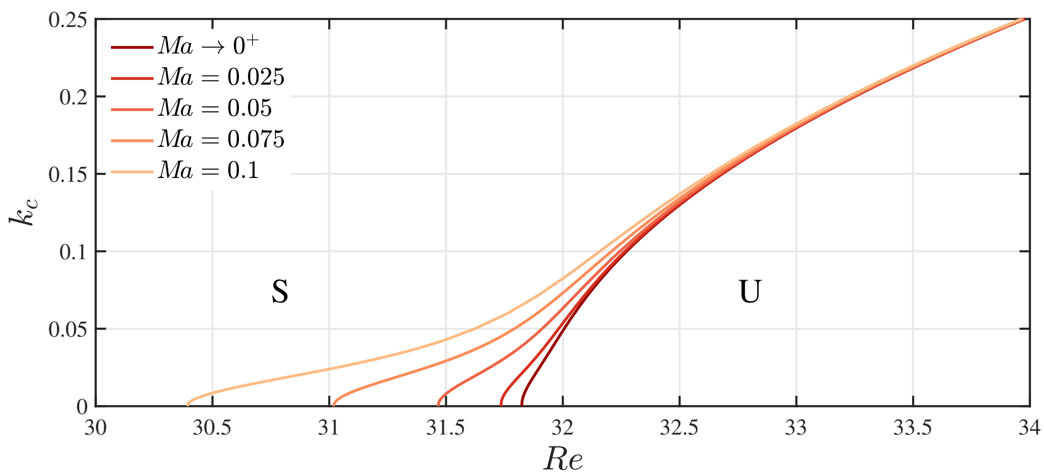

Figure 3: Impact of compressibility on the neutral stability diagram displaying the dimensionless cut–off wavenumber k_c as a function of the Reynolds number Re, for different small values of the Mach number Ma, shown in the legend. Parameter values: $g = 9.81\,\mathrm{m\,s^{-2}}$, $\beta = 1.5°$. Fluid physical properties – related to a falling film consisting of a water–glycerin mixture – are taken from Liu and Gollub (1994): $\tilde{\rho}_0 = 1070\,\mathrm{kg\,m^{-3}}$, $\tilde{\mu}_0 = 6.72\,10^{-3}\,\mathrm{Pa\,s}$, $\tilde{\gamma}_0 = 67.0\,10^{-3}\,\mathrm{N\,m^{-1}}$. The *stable* and *unstable* domain in the (Ma, Re) plane corresponds to areas labelled, respectively, “S” and “U”.

our study. The growth rate $k\,c_i(k)$ shown in figure 2*b* deviates upwards and towards increasing cut–off wavenumber k_c for growing Ma. Thus, compressibility plays a destabilising role on linear free–surface waves.

Even more distinctly, we observe this feature in figure 3, which shows the curve of marginal stability obtained for different values of the Mach number in the (Re, k_c) plane for $\beta = 1.5°$. Above the marginal stability curve, perturbations of wavenumber k decay in time, whereas they are amplified below. Here, the unstable region systematically undergoes a non–linear enlargement up to a smaller critical Reynolds number Re_{cr} due to the compressibility.

In order to quantify this shift into the stability threshold, we can examine the first–order expansion of the wave celerity $c^{(1)}$, which for $Ma \ll 1$ yields the following relation

$$Re_{cr} = \frac{5}{6}\left(1 - \frac{9}{2}\,Ma^2\right)\cot\beta, \tag{36}$$

obtained by making Re explicit from (34b) when the neutral stability condition $k\,c_i\,(k_c) = 0 \Longleftrightarrow c^{(1)}\big|_{Re_{cr}} = 0$ is imposed. In the limit of null Mach number, equation (36) reduces to the result of Benjamin (1957) and Yih (1963), *i.e.*, $Re_{cr}^{Ma\to 0^+} = 5/6\,\cot\beta$. Conversely, we observe that for $Ma = O(\varepsilon) > 0$ the compressibility lowers the critical Reynolds number Re_{cr} by a factor equal to

$$\frac{Re_{cr}\,(Ma)}{Re_{cr}^{Ma\to 0^+}} = 1 - \frac{9}{2}\,Ma^2 < 1, \tag{37}$$

anticipating the flow primary instability. This effect tends to asymptotically vanish in highly inertial regimes, within which compressible curves visibly become rapidly convergent towards the incompressible marginal stability plot (right–most line in figure 3). This finding is consistent as both the two compressible coefficients (31a) of the eigen–problem (30) are inversely proportional to the Reynolds number or its square power. Interestingly, we remark that the ratio expressed by (37) is independent of the plate inclination β.

5.2. Parametric analysis

Aiming at understanding the basic effects of compressibility on the film destabilisation, we investigate how the growth rate of disturbances $k\,c_i$ evolves as the parameter space, namely $\langle Re,\ \beta,\ We,\ Ma\rangle$, is explored. This will enable us to understand the fundamental physical mechanism through which compressibility acts, which we examine more in depth in § 6.

We start by providing a variety of numerical solutions to the linear stability problem (30) within the plane $(k,\, k\, c_i)$, for different values of the Reynolds number Re and angle of inclination β. Equations (34) suggest that a polynomial–type dependence is established by the novel Ma^{2j}–related contributions, namely $\Gamma_{2j}^{(n)} \cot^j \beta$. Unfortunately, the coefficients $\Gamma_{2j}^{(n)}$ display a fairly cumbersome functional dependence on $\cot\beta$ (as well as on Re) – apart from when $j = n$. For this reason, notwithstanding that the compressibility has no impact on a vertical falling film, it is not possible to determine *a priori* whether its effects varies with the inclination. Therefore, we will extensively cover the full range of variability in β, starting by focusing on mildly tilted configurations.

In figure 4 we initially consider four cases, denoted with letters (a–d), which differ from each other in terms of slope. To draw an appropriate comparison among these scenarios between each compressible curve ($Ma =$ 0.1 – dashed lines) and its incompressible counterpart (solid lines), the so–defined Reynolds critical ratio RCR

$$\mathrm{RCR} \overset{\mathrm{def}}{=} \frac{Re}{Re_{cr}^{Ma\to 0^+}} \tag{38}$$

is introduced as an inertia–based parameter. Four growing values of RCR are considered in each of the panels of figure 4, starting from a value which is numerically less than unity – which indicates a stable situation for a perfectly incompressible falling film flow – before moving to values of Re which progressively exceed the critical incompressible threshold.

As expected, the augmentation of RCR is associated with the extension of the instability region $c_i(k) > 0$. When we switch from each incompressible plot to its compressible analogue, the rightwards shift of the cut–off wavenum-

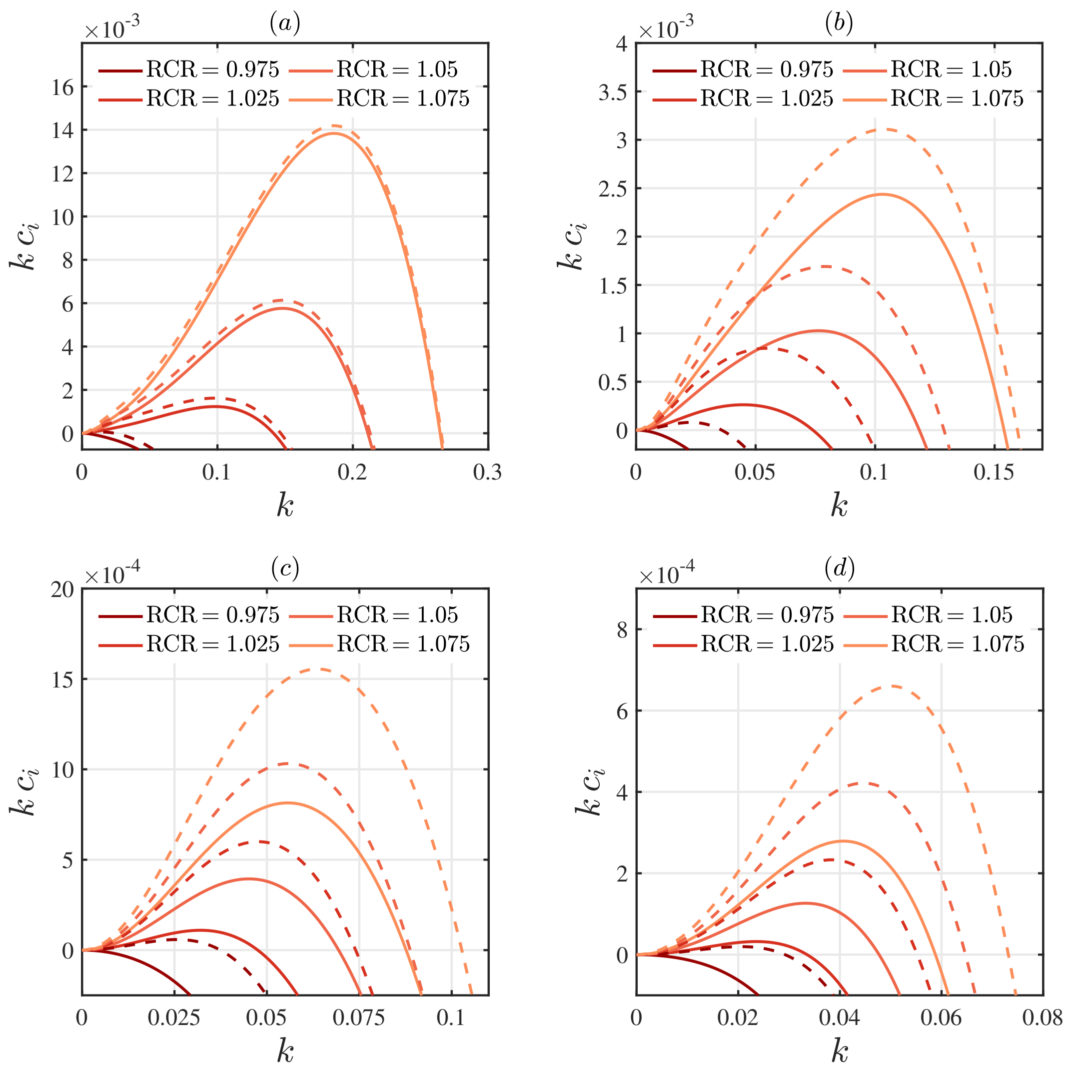

Figure 4: Effect of the Reynolds critical ratio RCR (38) (shown in the legend) on the graphical representation of the solution to the dispersion relation (32) for the derived weakly–compressible second–order model (25), in terms of the dimensionless imaginary growth rate $k\,c_i$ as a function of the dimensionless wavenumber k, for flow configurations which differ from each other in the value of the inclination angle β: (a) $\beta = 1.5°$, (b) $\beta = 3.0°$, (c) $\beta = 6.0°$, (d) $\beta = 12.0°$. The axes are dimensionless. Solid lines: $Ma \to 0^+$ (incompressible case), dashed lines: $Ma = 0.1$. Apart from the tilt angle β, other parameter values and fluid physical properties employed here are those of figure 3.

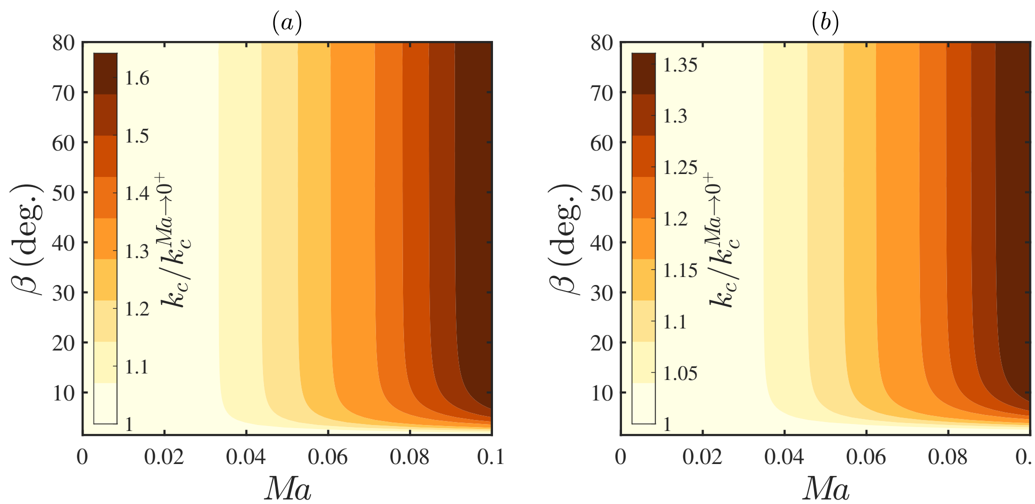

Figure 5: Effect of the Mach number $Ma = O(\varepsilon)$ and of the angle of inclination β on the stability of a falling water–glycerin film in terms of deviation of the cut–off wavenumber k_c from its incompressible limit $k_c^{Ma\to 0^+}$ with reference to the temporal growth rate of linear disturbances $k\, c_i(k)$, for two different fixed values of the Reynolds critical ratio (38), corresponding to (a) RCR $= 1.025$ and (b) RCR $= 1.05$. In overall terms, darker regions correspond to a greater destabilisation. The set of parameter values and fluid physical properties is the same specified for figure 3.

ber k_c is reduced as the RCR is raised. This is in accordance with what previously shown in figure 3. As the incline of the plate becomes steeper, provided that moderately low–angle configurations are explored, the compressibility plays an increasingly important effect in relative terms in terms of a rightward shift of the dispersion curves.

In order to better appreciate this phenomenon, we represent in figure 5 the contours of the cut–off wavenumber related to its incompressible limit $k_c/k_c^{Ma\to 0^+}$ as a function of the Mach number Ma and of the inclination angle β for two different values of Reynolds critical ratio RCR beyond the stability threshold, corresponding to (a) RCR $= 1.025$ and (b) RCR $= 1.05$, respectively. In both scenarios we identify two distinct regions of the (Ma, β) plane: (i) a low–angle region ($1.5° \lesssim \beta \lesssim 12°$) where compressibility–induced destabilisation is not fully–developed in terms of rightward shift of the cut–off wavenumber and (ii) a region that covers moderately to highly tilted configurations ($12° \lesssim \beta \lesssim 80°$), where the same effects are independent of the value of inclination angle β. From a graphical point of view, the isolines rapidly tend to become vertical, indicating a fast saturation of $k_c/k_c^{Ma\to 0^+}$ with respect to slope.

Within area (ii), at $Ma = 0.1$ – the highest level of weak compressibility investigated – the cut–off wavenumber is increased by up to roughly 60% when RCR$= 1.025$ and 35% when RCR$= 1.05$ in comparison with the incompressible case. As it will soon become clear, there exists a third upper region (iii) – for $80° \lesssim \beta \leq 90°$ – which is difficult to explore by employing the parameter RCR since, there, a vertically falling film flow is always unstable to linear perturbations (Benjamin, 1957; Yih, 1963).

A similar behavior is shown by the most unstable wavenumber and the maximum growth rate of linear disturbances related to their incompressible limit, *viz.* $k_{\max}/k_{\max}^{Ma\to 0^+}$ and $\omega_{i,\max}/\omega_{i\max}^{Ma\to 0^+}$ respectively, which are displayed in figure 6*a,b* as a function of the Mach number Ma and the inclination angle β in the case of a Reynolds critical ratio equal to RCR $= 1.05$. The results are shown up to $\beta = 40°$, as the isocontour does not change in the region $40° < \beta < 80°$, as discussed before. The most unstable wavenumber increases up to 35% compared with its incompressible analogue. Also, the compressibility induces a similar increase of $k_c/k_c^{Ma\to 0^+}$ and $k_{\max}/k_{\max}^{Ma\to 0^+}$,

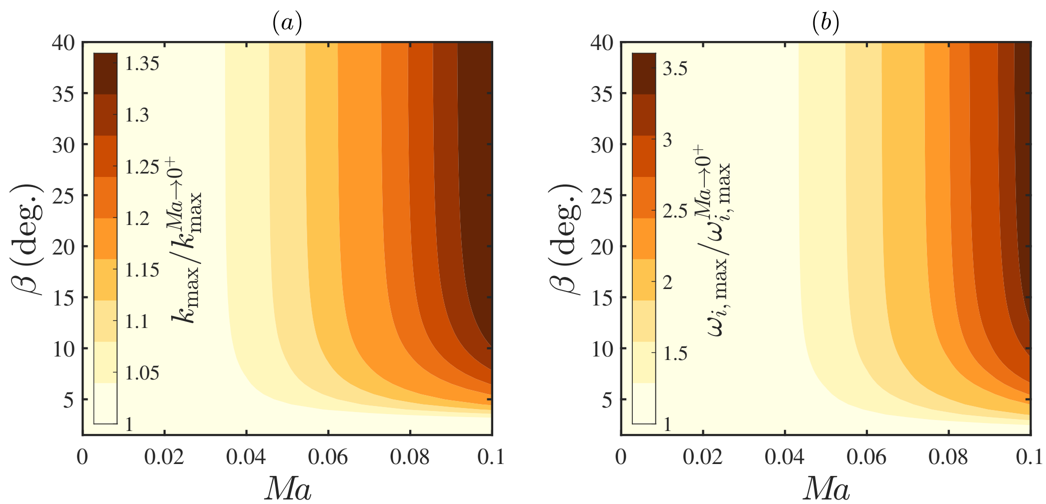

Figure 6: Effect of the Mach number $Ma = O(\varepsilon)$ and of the angle of inclination β on the stability of a falling water–glycerin film. Deviation of (a) the most unstable wavenumber $k_{\max}$ from its incompressible limit $k_{\max}^{Ma\to0^+}$, (b) the maximum growth rate $\omega_{i,\max}$ from its incompressible limit $\omega_{i,\max}^{Ma\to0^+}$ for a value of Reynolds critical ratio (38) equal to $\mathrm{RCR} = 1.05$. In overall terms, darker regions correspond to a greater destabilisation. The set of parameter values and fluid physical properties is the same specified for figure 3.

as shown in figures 6a and 5b, indicating that the destabilization involves both long and relatively short waves. Meanwhile, the maximum growth rate $\omega_{i,\max}$ can reach values up to about three and a half times higher than the incompressible one.

A method to explore the role of compressibility at highly–tilted configurations consists in predetermining an adequate value of Re. For such a selection, we chose to cover a reasonably broad spectrum of slopes (with special attention to the steepest ones), without dropping the shallowness assumption.

Figure 7 displays the contours of the normalised cut–off wavenumber as a function of the Mach number and of the inclination angle for two different fixed values of the Reynolds number, corresponding to (a) $Re = 1$ (with β ranging between $60°$ and $90°$) and (b) $Re = 3$ (with $20° \leq \beta \leq 60°$). These combination of (Re, β) is such as to determine the onset of interfacial instability. From panels a–b, one may erroneously infer that, as β increases, $k_c/k_c^{Ma\to 0^+}$ exhibits a diminishing trend in contrast with previous results. However, this evolution is fully justifiable in the following terms: keeping Re fixed while the solid substrate steepens is tantamount to moving further away from the critical threshold, which corresponds to a progressive augmentation of the Reynolds critical ratio RCR, that is a situation where the compressibility–related effects on the destabilisation are less significant. As a consequence, figure 7 is consistent with what displayed in figures $3, 5$ and, besides, helps in extending our analysis to the case of a vertical falling film flow.

As final part of the parametric study our sole aim is to investigate the influence of the Weber number We – and thus of the surface tension – on the compressibility–induced destabilising mechanism. To do so, we conclude by presenting numerical results for three different fluids: (i) water, (ii) aqueous solution of dimethylsulfoxide (DMSO), and (iii) aqueous solution of glycerin. As summarised in table 1, these fluids display different physical properties in terms of density, kinematic viscosity and surface tension, notwithstanding that the adopted barotropic EoS (14) remains unaltered among them. As regards the other variables belonging to the parameter space, the angle of inclination and the Reynolds critical ratio have been kept fixed and equal to $\beta = 15°$ and RCR$=$ 1.05, respectively. Such a choice corresponds to

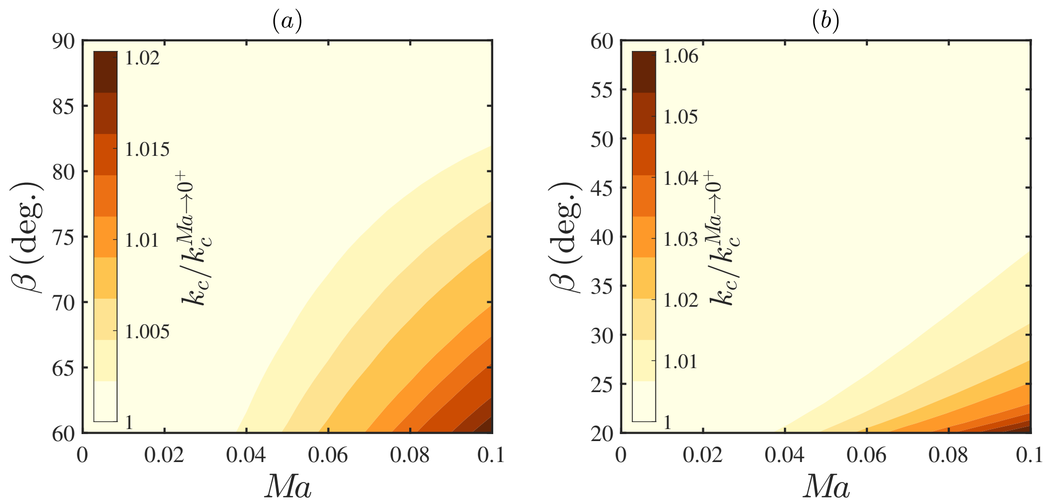

Figure 7: Effect of the Mach number $Ma = O(\varepsilon)$ and of the angle of inclination β on the stability of a falling water–glycerin film in terms of deviation of the cut–off wavenumber k_c from its incompressible limit $k_c^{Ma\to 0^+}$ with reference to the temporal growth rate of linear disturbances $k\,c_i(k)$, for two different fixed values of the Reynolds number, corresponding to (a) $Re = 1$ and (b) $Re = 3$. In overall terms, darker regions correspond to a greater destabilisation. The set of parameter values and fluid physical properties is the same specified for figure 3.

Fluid	$\tilde{\rho}_0$ ($\mathrm{kg\,m^{-3}}$)	$\tilde{\nu}_0$ ($10^{-6}\,\mathrm{m^2\,s^{-1}}$)	$\tilde{\gamma}_0$ ($10^{-3}\,\mathrm{N\,m^{-1}}$)	Ka
Water	1000.0	1.00	76.9	3592
DMSO (83.11%)	1098.3	2.85	48.4	509.5
Glycerin (50%)	1130.0	5.02	69.0	331.8

Table 1: Physical properties of fluids considered in the numerical stability calculations. The working liquids are the same as in Lavalle et al. (2019) (table 3 there): water, an aqueous solution of DMSO at 83.11% by weight, and an aqueous solution of glycerin at 50% by weight. The Kapitza number Ka is defined as $Ka = \tilde{\gamma}_0 \left(\tilde{\rho}_0\, g^{1/3}\, \tilde{\nu}_0^{4/3}\right)^{-1}$, being $\tilde{\nu}_0 = \tilde{\mu}_0/\tilde{\rho}_0$ the kinematic viscosity of the fluid under consideration.

the following set of values for the Weber number: (i) $We = 8.841\ 10^{-4}$, (ii) $We = 6.234\ 10^{-3}$, (iii) $We = 1.156\ 10^{-2}$. We have represented in figure 8 the cut–off wavenumber (a) and the maximum growth rate (b) as a function of the Mach number Ma for the three liquids considered. As before, in both panels the quantities shown are related to their analogues in the limit of a perfectly incompressible flow. Within the present weakly compressible scenario, we see that the onset of the long–wave instability is dimly affected by surface tension and the destabilising effect of compressibility is felt earlier at low Weber numbers.

6. Physical basis for the destabilising effect of compressibility

This section aims at clarifying the underlying physics behind the compressibility effect on the onset of the flow primary instability.

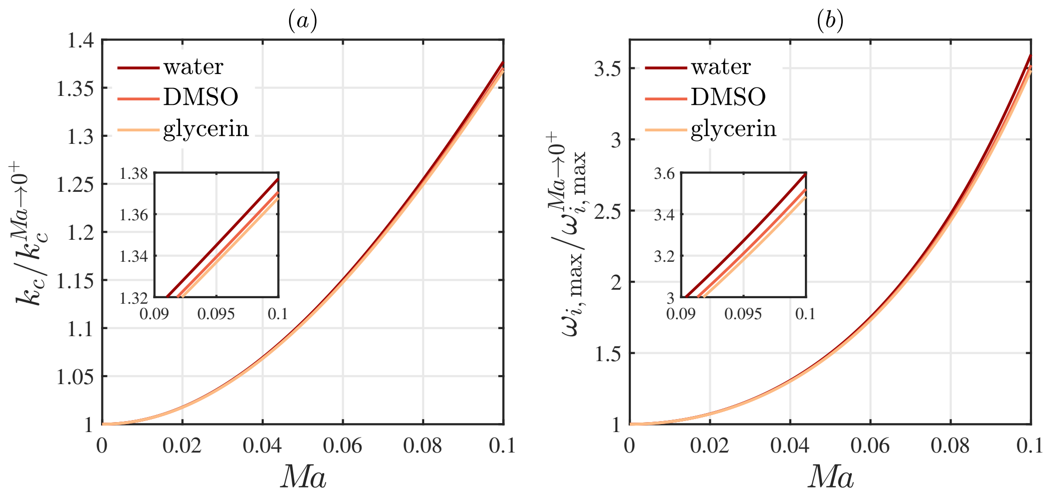

Figure 8: Effect of the Mach number $Ma = O(\varepsilon)$ on the stability of three falling film flows, each obtained employing one of the fluids detailed in table 1 in terms of physical properties and listed in the legend. Curves represent the deviation of (a) the cut–off wavenumber k_c from its incompressible limit $k_c^{Ma\to 0^+}$ and (b) the maximum growth rate $\omega_{i,\,\mathrm{max}}$ from its incompressible limit $\omega_{i,\,\mathrm{max}}^{Ma\to 0^+}$ with reference to the temporal growth rate of linear disturbances $\omega_i(k) \equiv k\, c_i(k)$, for a fixed value of the Reynolds critical ratio (38), equal to $\mathrm{RCR} = 1.05$, and inclination angle $\beta = 15°$.

6.1. Whitham wave hierarchy

The hydrodynamic stability of a shallow–water flow is linked to the propagation of interfacial waves (Whitham, 1974; Alekseenko et al., 1985, 1994; Ooshida, 1999; Kalliadasis et al., 2013). In this respect, Whitham's theory of two–wave competition serves as a framework to interpret the linear stability properties of the depth–averaged weakly–compressible model (25). To do so, we can make use of the dispersion relation (32) to study the mechanism at the base of the compressible–induced destabilisation. Specifically, we formally recast (32) into the canonical form

$$i\,(c - c_k)\, + \Omega\, k\,(c - c_{d^+})\,(c - c_{d^-}) = 0, \tag{39}$$

where $c_k\,(k^2; Re,\, \beta,\, We,\, Ma)$, $c_{d^\pm}\,(k^2; Re,\, \beta,\, We,\, Ma)$ and $\Omega\,(k^2; Re)$ are defined as follows

$$c_k = \frac{3}{2\,k^2+3}\left[3 + k^2\left(-1 - \frac{4}{7}\,Re\cot\beta + \frac{24}{35}\,Re^2 - \frac{3}{Re}\,Ma^2\cot\beta\right) - \frac{4}{21}\,\frac{Re^2}{We}\,k^4\right] \tag{40a}$$

$$c_{d^\pm} = -\frac{9\,Ma^2\,\cot\beta}{4\,Re} \pm \frac{1}{2}\sqrt{\frac{4\,k^2}{We} + \frac{12\,\cot\beta}{Re} + \frac{108}{5} + \frac{81\,Ma^4\,\cot^2\beta}{4\,Re^2}} \tag{40b}$$

$$\Omega = \frac{Re}{2\,k^2+3}. \tag{40c}$$

Since the dispersion relation (39) recalls a two–wave structure, our reduced model (25) can be systematically reinterpreted as a second–order wave equation

$$\underbrace{(\partial_t + c_k\,\partial_x)\,h}_{\text{(i)}} + \Omega\,\underbrace{(\partial_t + c_{d^-}\,\partial_x)\,(\partial_t + c_{d^+}\,\partial_x)\,h}_{\text{(ii)}} = 0, \tag{41}$$

which consists of two levels (i) (ii) of linear hyperbolic wave equations. The lower–order solutions to (i) are the *kinematic* waves since they origin from the mass conservation (25a). These fast waves travel at a speed equal to c_k and they are dominant at long time and in the inertia–less limit $\Omega(Re) \to 0^+$. Conversely, the higher–order *dynamic* waves of the second kind (ii) arise from the film response, governed by the stress continuity condition (10b – 10c) or – equivalently – by the momentum balance (25b), to variations in momentum, hydrostatic pressure and surface tension. They correspond to the limit $\Omega(Re) \to +\infty$. In their early stage, wavefronts located at the leading front and at the trailing edge of a produced wave packet begin to travel at a speed equal to c_{d^+} and c_{d^-}, respectively.

Interestingly, the dependence of $\Omega(k)$ on the wavenumber k is a mere consequence of the non–hyperbolicity of the evolution equation appertaining to the integral model (25), since terms whose order of spatial derivation exceeds the second would be ultimately included in it (Ruyer-Quil, 2012; Kalliadasis et al., 2013). Physically, this means that surface wave dispersion is modified by the streamwise viscous diffusion as early as the instability onset (Sharma and Dandapat, 2006). Anyway, $\Omega(k^2)$ is not appreciably affected by the squared wavenumber k^2. In fact, by inspection of (40c), the denominator $2\,k^2 + 3 \approx 3$ within the long–wave limit ($k \ll 1$). As an *a posteriori* argument, this fact adds legitimacy to the assumption of virtually non–dissipative fluid (Samanta et al., 2011), postulated in § 3.1 behind the adoption of (14) as barotropic EoS. The dependence (40a) of the kinematic wave speed c_k on the squared wavenumber k^2 gives an estimate of the dispersive role of the streamwise second–order viscous terms, sometimes referred to as "viscous dispersive effect" (Ruyer-Quil et al., 2008).

6.1.1. *Two–wave reframing of the critical threshold*

Whitham (1974) proved that the film primary instability can be precisely reasoned in terms of competition between kinematic and dynamic waves. Whenever a multi–speed equation of the kind given in (41) holds, long–wave interfacial disturbances will damp on the condition that kinematic waves travel at a speed ranging between the speeds of dynamic waves:

$$c_{d^-} \leq c_k \leq c_{d^+}. \tag{42}$$

The origin of the temporal stability criterion (42) stems from the evolution of a localised precursory ripple (Ruyer-Quil, 2012). Since kinematic waves tend to emerge from the wave packet at long times, whereas its short–term dynamics is dominated by dynamic waves, the only stable situation is one where the back and front of the wave travel at dynamic wave speed c_{d^-} and c_{d^+} respectively, which implies constraint (42). The base state is marginally stable if $c_{d^-} = c_k$ or $c_{d^+} = c_k$. Here, in practice, only the latter condition has a binding character on the inception of the flow instability. Once evaluated in the limit of infinitely long waves ($k \to 0^+$), it is verified that equality:

$$c_{d^+} = c_k \tag{43}$$

is coherently able to recover (36), thus being in line with the expression for the neutral stability threshold previously found by means of an asymptotic expansion *à la* Yih (1963) for the wave celerity $c(k)$.

6.1.2. *Elucidation of the compressibility–induced destabilising effect*

To illustrate how compressibility enters Whitham's paradigm, we follow the methodology adopted by Samanta et al. (2011) and Samanta (2014) for liquid films falling along a slippery incline or in the presence of imposed shear stress, respectively. We consider the scenario discussed in figure 4(a, d), *i.e.* a water–glycerin film down a plane inclined at $\beta = 1.5°$ and $\beta = 12°$. For these two angles of inclination, figure 9 compares the kinematic wave speed c_k and the dynamic one c_{d^+} given by (40a) and (40b) as a function of the squared dimensionless wavenumber k^2, both within the incompressible limit $Ma \to 0^+$ (solid lines) and in a slightly compressible case, where $Ma = 0.1$ (dashed lines). Two values of the Reynolds critical ratio RCR – beyond the stability threshold, though in its vicinity – have been examined: (a, c) RCR$= 1.025$ and (b, d) RCR$= 1.075$.

Figure 9 evidences that the compressibility contributes in lowering both the dynamic and the kinematic wave speeds. For further clarification, figure 9 has been completed with a proper close–up of the plane portion where curves cross each other. One easily realizes that each compressible cut–off point (void circle) is always located at a higher squared wavenumber k^2 in comparison with its incompressible analogue (filled circle).

The kinematic wave speed c_k, however, is much less affected by the compressibility than the dynamic one c_{d^+}. This can be inspected by a brief discussion on the role of inertia. Let us first consider the low–angle configuration (upper panels). In such a scenario, the variation in the Reynolds critical ratio RCR in figure 9a,b seems to only have a minor impact on the compressible dynamic celerity c_{d^+} in terms of vertical shift. On the other hand, for the greatest RCR (panel b), the parabolic–like trend of the kinematic celerity c_k evolves with respect to k^2 in such a way that its descending tract gets drastically steeper in the vicinity of its point of intersection with the graph of the

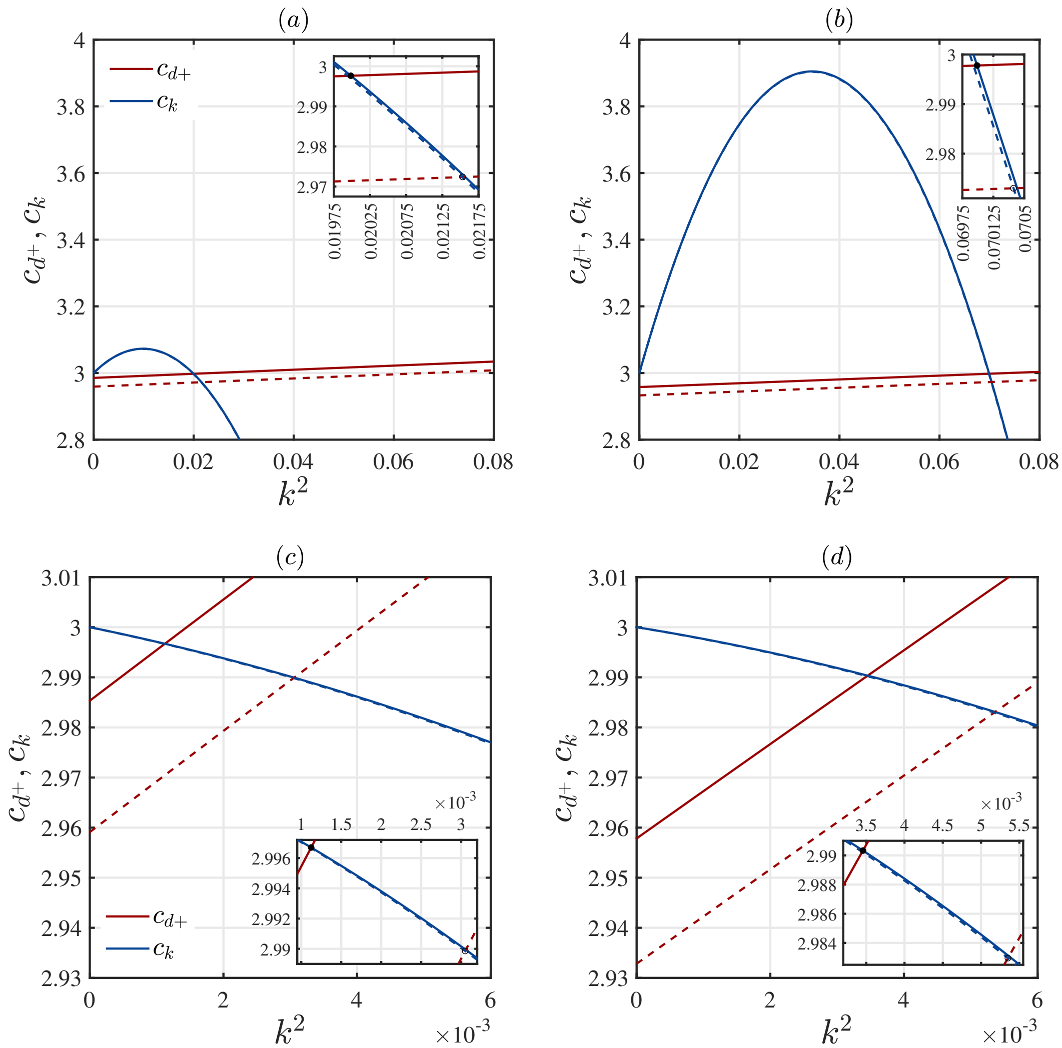

Figure 9: The variation of dynamic c_{d^+} (in red) and kinematic c_k (in blue) wave speeds as a function of k^2 when the Mach number Ma passes from zero (solid lines) to a value of 0.1 (dashed lines), for different configurations in terms of angle of inclination β and Reynolds critical ratio RCR. (*a*–*b*): $\beta = 1.5°$. (*c*–*d*): $\beta = 12°$. Left panels: RCR $= 1.025$. Right panels: RCR $= 1.075$.

dynamic wave velocity c_{d^+}. As a consequence, the compressibility–induced destabilisation gets noticeably reduced when the Reynolds number increases.

We close this section by comparing panels $(c-d)$, for which the inclination angle is $\beta = 12°$. Here we notice that the speed of kinematic waves c_k is less sensitive in comparison with the previous low–angle configuration to the same increase in the Reynolds critical ratio, from RCR$=$ 1.025 (left) to RCR$=$ 1.075 (right). Meanwhile, the dynamic wave speed c_{d^+}, which increases as a straight line with the square of the wavenumber k^2, undergoes deceleration by enhancing compressibility, but also by increasing RCR, leading to an attenuation of the compressibility–induced destabilisation.

6.2. Impact of compressibility on flow–related quantities

Aiming at finding a physical source to which the overflow uncovered in § 4.1.1 may be attributed, we rephrase the pertinent perturbative analogue $\Delta\, q^{(2)}_{\mathrm{rel}} = \left(q^{(2)} - q^{(2)}\big|_{Ma\to 0^+}\right)/q^{(0)}$ in terms of dimensional variables, which gives:

$$\Delta\, q^{(2)}_{\mathrm{rel}} = \frac{\Lambda}{8}\frac{g\,\tilde{h}\,\cos\beta}{\tilde{a}_0^2}. \tag{44}$$

In a similar way, as the leading–order wall shear stress $\tau_w^{(0)} \equiv \partial_y u^{(0)}\big|_{y=0}$ is employed as normalising quantity for the extra wall shear stress profile, we obtain:

$$\Delta\, \tau^{(2)}_{w,\,\mathrm{rel}} = \frac{\Lambda}{6}\frac{g\,\tilde{h}\,\cos\beta}{\tilde{a}_0^2}. \tag{45}$$

The same functional form is manifestly shared by (44) and (45). A simple physical interpretation of the ratio therein contained, namely $g\,\tilde{h}\,\cos\beta/\tilde{a}_0^2$, can be given in the following terms:

$$\Delta\, q^{(2)}_{\mathrm{rel}},\, \Delta\, \tau^{(2)}_{\mathrm{rel}} \propto \frac{\tilde{\rho}\,g\,\tilde{h}\,\cos\beta}{\tilde{\rho}\,\tilde{a}_0^2} = \frac{\tilde{P}^{\mathrm{eff}}_{\mathrm{h}}}{\tilde{P}_{\mathrm{a}}}. \tag{46}$$

We can notice that (46) accounts for the ratio between the effective component of the hydrostatic pressure $\tilde{P}_{\mathrm{h}}^{\mathrm{eff}}$ exerted along the cross–stream direction by the wavy fluid column of height $\tilde{h}$, as stipulated by Stevin's law, and a reference acoustic pressure $\tilde{P}_{\mathrm{a}}$. As a matter of fact, the whole operating mechanism through which compressibility acts as a destabilising factor for the temporal development of long–wave linear disturbances should be intended as the competition of multiple effects: for decreasing angles of inclination, the gravitational effect is emphasised as $\cos\beta$ increases, but such a trigger for destabilisation is counterbalanced by the decrease of the uniform film thickness $\tilde{h}_N$, which is a function of $\sin\beta$, and so of $\tilde{h}$.

6.2.1. Compressible lag of flow rate perturbations

In order to explain the physical mechanism responsible for the compressibility–induced flow destabilisation, we adapt the basic rationale behind the methodology followed by Lavalle et al. (2019) in the context of confined falling liquid films in presence of an active upper phase. We start by recalling that the driving mechanism of Kapitza instability can be traced back to inertia, which is responsible for the time lag between the actual liquid flow rate $q\,(h(x,\,t))$ and its inertialess target value:

$$q^{\star}(h(x,\,t)) = \underbrace{\frac{\Lambda\, h^3}{3}}_{q^{\star,\,g}} + \underbrace{\frac{Ma^2\, h^4\, \Lambda^2 \cot\beta}{8\, Re}}_{q^{\star,\,Ma}} + O(\varepsilon^2). \tag{47}$$

Here the second–order contribution arising from the flow compressibility has been highlighted individually, without expressly taking its limit as $Re \to 0^+$ owing to its divergent behaviour. Instead, two other Re–independent second–order terms contained within the expression of $q^{(2)}$ and arising in particular

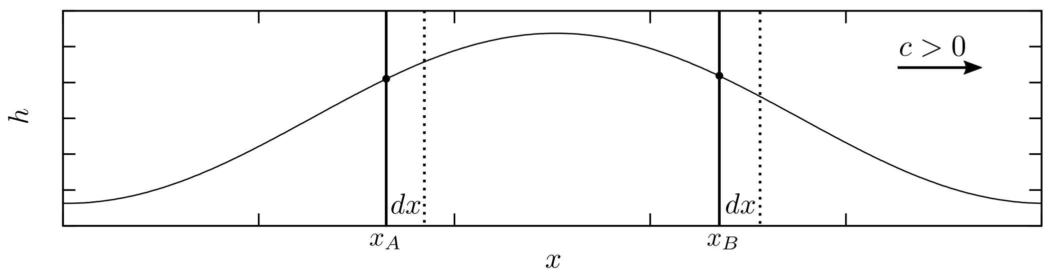

Figure 10: Description scheme of the inertia–based mechanism of the Kapitza instability: by comparison between two points of abscissa x_A and x_B, located at opposite sides of a wave peak, the local film flow rate $q(x, t)$ is delayed in accommodating itself to film thickness variations induced by the passage of the superficial disturbance of speed c.

from the normal stress continuity condition (10b) at order $O(\varepsilon^2)$ have not been explicitly written in (47) and disregarded for simplicity in subsequent calculations. Such a decomposition therefore appears to be accurate at $O(\varepsilon)$ and it is used only as a means to gain insight at the mechanism at work by estimating the relative importance of each individual component in the destabilisation of the weakly–compressible flow.

The destabilising role of inertia on single–peaked Kapitza waves can be explained resorting to the analysis followed by Dietze (2016), who considered the history of two points located along the film free–surface either side of a wave crest. With reference to figure 10, at the abscissa x_B upstream of the wave hump, where $\partial_x h < 0$, the film thickness increases in time as the wave covers a distance dx, and so does the flow rate q along the x direction, in accordance with Benney's leading–order asymptotic expansion (B.1c). Conversely, at the abscissa x_A downstream of the wave hump, the film thickness and the flow rate decrease when the wave covers dx. In the presence of inertia, the flow rate cannot adapt instantaneously to such a film thickness variation. As a result, the flow rate in x_A will be too high while it will be too low in x_B. The ensuing discrepancy in flow across the wave peak accounts for its growth. Such a response is more intense as the lag phase of the actual flow rate q behind its target value $q^\star$ increases.

According to (47), the effect of gravity through the cubic dependence of $q^{\star,\,g}\,(h)$ on h tends to promote variations in $q^\star$ between the wave hump and the wave trough as an outcome of the change in film thickness h. The non–negative compressible contribution $q^{\star,\,Ma}\,(h)$ exacerbates such an effect, increasingly so as the corresponding term in (47) gains relevance. For a pertinent quantification, variables appearing in equation (47), *viz.* the wavy film thickness h and the inertialess film flow rate $q^\star$, are linearly perturbed around the aforediscussed (see § 4.1.1) base state vector $\mathbf{Q}_0$, via superimposition of infinitesimal disturbances of amplitude $\|\hat{\mathbf{Q}}\| \ll \|\mathbf{Q}_0\|$:

$$h\,(x,\,t) \,=\, h_0 + \hat{h}\,(x,\,t) \tag{48a}$$

$$q^\star(h) \,=\, q_0 + \hat{q}\,(h)\,. \tag{48b}$$

By virtue of (48) it is now possible to discriminate between the magnitude of perturbations $\hat{q}^g$ and $\hat{q}^{Ma}$, which are, respectively, of gravitational and compressible provenance:

$$\hat{q}\,(\hat{h}) = \underbrace{\Lambda\,h_0^2\,\hat{h}}_{\hat{q}^g} + \underbrace{\frac{Ma^2\,h_0^3\,\hat{h}\,\Lambda^2\cot\beta}{2\,Re}}_{\hat{q}^{Ma}}\,. \tag{49}$$

The following expression can be obtained for the so–defined compressible–to–total amplitude ratio $\hat{q}^{Ma}/\hat{q}$:

$$\left|\frac{\hat{q}^{Ma}}{\hat{q}}\right| = \frac{3\,Ma^2\,\cot\beta}{2\,Re + 3\,Ma^2\,\cot\beta} \overset{(*)}{=} \frac{9\,Ma^2}{5\,\mathrm{RCR} + 9\,Ma^2}, \tag{50}$$

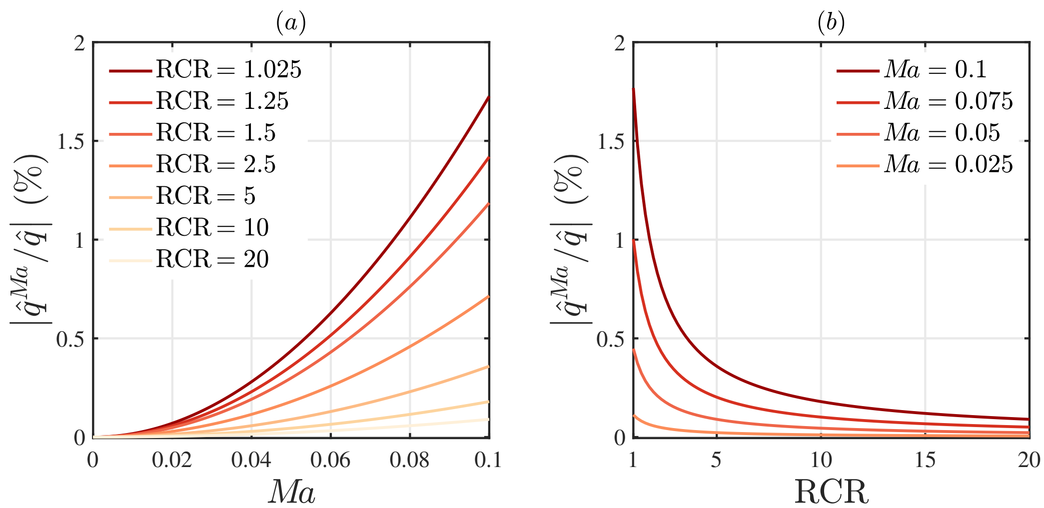

Figure 11: Percentage contribution of the compressibility–related perturbation $\hat{q}^{Ma}$ to the total inertialess flow rate perturbation $\hat{q}$ (49) (a) as a function of the Mach number $Ma = O(\varepsilon)$ for different fixed values of the Reynolds critical ratio RCR (displayed in the legend) and (b) *vice versa*.

in which use has been made of the equality $\Lambda = 3$ and of the identity $h_0 \equiv 1$, ($*$) together with the definition of the Reynolds critical ratio RCR (38), coupled with the incompressible evaluation of the critical threshold $\lim_{Ma\to 0^+}$(36), in lieu of the Reynolds number Re. Figure 11 shows that the ratio expressed by (50) (a) increases with the Mach number Ma and (b) decreases with the Reynolds critical ratio RCR, which is in accordance with the most prominent role played by compressibility in the film flow destabilisation shown in section § 5.

7. Conclusions

Liquid films occur over a wide range of length scales and are central to numerous areas of pure and applied sciences (Craster and Matar, 2009).

The development of long–wave instabilities along its interface leads to self–excitation of non–trivial dynamics (Sharma and Dandapat, 2006). The motivation behind this study is addressing theoretically how changes in the fluid density fit into this context. For such purpose, we have discussed three guiding questions.

(i) How does compressibility affect the structure of a depth–integral model? We considered a barotropic relation involving the Mach number of the mean flow. Under the assumption of weak compressibility $Ma \ll 1$, the density of the fluid is found to be exponentially stratified against gravity along the crosswise direction. In the final depth–averaged system (25) this is reflected in two additional terms: one $\propto \cot\beta\, Ma^2/Re$ in the continuity equation, and the other $\propto \cot\beta\, Ma^2/Re^2$ in the momentum conservation equation.

(ii) To what extent does compressibility take part in long–wave instability? According to our linear analysis, a low degree of compressibility boosts the inception of interfacial instability. This effect is most marked in low–inertial regimes. For instance, with reference to figure 5*b*, the instability threshold of a water–glycerin film flow having $Re = 2.40$, $\beta = 20°$ and $Ma = 0.1$ as set of distinctive parameters is seen to increase by 35% in terms of the cut–off wavenumber with respect to its incompressible analogue. A higher–order additive correction of the base flow rate, hydrostatic in nature, has been highlighted via (44). As perspective on future research, the derived depth–integrated model (25) will be also of interest to simulate the non–linear dynamics of weakly–compressible falling liquid films, on condition that proper manipulations are performed for the numerical treatment of capillary terms (Lavalle et al., 2015).

(iii) Which is the underlying physical foundation? Albeit of small magnitude, differences between the compressible and incompressible nature of the long–wave instability can be traced back to a compressible–induced deceleration of dynamic waves (figure 9) or, equivalently, to an additional inertia–induced delay (relative to the kinematic waves) of the flow rate in adapting to a time–varying film–thickness (figure 11).

Acknowledgements

Authors record their sincerest gratitude for financial support allocated during the course of this work by the Auvergne–Rhône–Alpes region as part of the project "MuscaFlow" (21 007147), agreed between Mines Saint–Etienne and Università di Brescia.

Declaration of interests

The authors report no conflict of interest.

Appendix A. Reduction of the pressure profile

The complete solution of (16) is given by:

$$
\begin{aligned}
p(x,y,t;\vartheta) = p_i + \frac{\overbrace{\exp\left[\dfrac{\cos\beta}{Fr} Ma^2\,(h-y)\right]}^{\blacklozenge} - 1}{Ma^2} - \frac{\varepsilon^2}{We}\partial_{xx}h \, + \\
+ \quad \frac{\varepsilon}{Re}\Bigg[\mathcal{W} - \mathcal{W}|_h \overbrace{\exp\left[\frac{\cos\beta}{Fr}Ma^2\,(h-y)\right]}^{\blacklozenge} - \left(\frac{2}{3} - \vartheta\right)\left(\partial_x u + \partial_y v\right)\big|_h \, + \qquad \text{(A.1)} \\
+\, 2\,(\partial_y v)|_h - 2\,\overbrace{\partial_x h\,(\partial_y u)|_h}^{\lozenge}\Bigg] - \mathcal{I}(y,\,\mathcal{W})\,\exp\left(-\frac{\cos\beta}{Fr}Ma^2\,y\right),
\end{aligned}
$$

where $\mathcal{I}(y,\,\mathcal{W})$ is the so–defined primitive

$$\mathcal{I}'(y,\,\mathcal{W}) = \varepsilon\, Ma^2\, \frac{\cos\beta}{Re\, Fr}\, \mathcal{W}\, \exp\left(\frac{\cos\beta}{Fr} Ma^2\, y\right), \tag{A.2}$$

the prime mark denoting total differentiation with respect to y. By inspection of (A.2), since it is assumed $Re \sim Fr = O(1)$, $\mathcal{I}'$ can be regarded as an $O(\varepsilon\, Ma^2)$ residual contribution, originating from the process of integration by parts in the context of the application of Duhamel's technique. Given that its analytical integration would at least require *a priori* knowledge concerning the explicit expression for the unknown spatial derivatives of the velocity field $\mathbf{v} = (u,\, v)$ involved within $\mathcal{W}$ as part of the integrand function (A.2), we seek for a low–compressibility restriction of the kind

$$\varepsilon\, Ma^2 \lesssim \varepsilon^3, \tag{A.3}$$

a condition wherein it is legitimate to consistently ignore its respective contribution within the ultimate problem (9) via (14). Indeed, assignment (A.3) has been formalised in asymptotic terms through the equivalence relation (19), with $\alpha \geq 1$ and $M = O(1) \in \mathbb{R}_0^+$. By recalling expansion (20) with (A.3) in mind, the $O(\varepsilon)$–exponential term denoted as $\blacklozenge$ can be shortened to the unitary value only. Furthermore, starting from the definition of $\mathcal{W}$ – jointly given with (16) – it is straightforward to verify that

$$-\left.\mathcal{W}\right|_h - \left(\frac{2}{3} - \vartheta\right) \left.(\partial_x u + \partial_y v)\right|_h + 2\left.(\partial_y v)\right|_h \equiv -\left.(\partial_x u)\right|_h . \tag{A.4}$$

Finally, the boundary condition (10c) highlights the fact that $\left.(\partial_y u)\right|_h = O(\varepsilon^2)$, thereby allowing for the removal of $\Diamond$, which ultimately contributes as an $O(\varepsilon^3)$ term within (A.1). As a result, (A.1) is consistently tantamount to (17).

Appendix B. Asymptotic expansions

Appendix B.1. Leading order $O(\varepsilon^0)$

$$u^{(0)}(h(x,t),y) = -\frac{\Lambda\,(y^2 - 2\,h\,y)}{2} \tag{B.1a}$$

$$v^{(0)}(h(x,t),y) = -\frac{\Lambda\,(\partial_x h)\;y^2}{2} \tag{B.1b}$$

$$q^{(0)}(h(x,t)) = \frac{\Lambda\,h^3}{3} \tag{B.1c}$$

The steady–state flat–film solution, corresponding to Nusselt flow (Nusselt, 1916), can be recovered by substituting unity for h in equations (B.1). This shows that the leading order of Benney's development corresponds to local equilibrium.

Appendix B.2. First order $O(\varepsilon^1)$

$$u^{(1)}(h(x,t),y) = \frac{Re\,\varepsilon^2}{We}\,\partial_{xxx}h\left(hy - \frac{y^2}{2}\right) + \frac{Re\,\cos\beta}{Fr}\,\partial_x h\left(-hy + \frac{y^2}{2}\right) +$$

$$+Re\,\Lambda^2\partial_x h\left(\frac{hy^4}{24} - \frac{h^4 y}{6}\right) + Re\,\Lambda\,\partial_t h\left(\frac{y^3}{6} - \frac{h^2 y}{2}\right) \tag{B.2a}$$

$$v^{(1)}(h(x,t),y) = \frac{Re\,\varepsilon^2}{We}\left[\partial_{4x}h\left(\frac{y^3}{6} - \frac{hy^2}{2}\right) - (\partial_x h)\,(\partial_{xxx}h)\,\frac{y^2}{2}\right] +$$

$$+\frac{Re\,\cos\beta}{Fr}\left[\partial_{xx}h\left(-\frac{y^3}{6} + \frac{hy^2}{2}\right) + \partial_x^2 h\,\frac{y^2}{2}\right] +$$

$$+Re\,\Lambda\,y^2\left[\partial_{tx}h\left(-\frac{y^2}{24} + \frac{h^2}{4}\right) + (\partial_t h)\,(\partial_x h)\,\frac{h}{2}\right] +$$

$$+Re\,\Lambda^2\left[\partial_{xx}h\left(-\frac{hy^5}{120} + \frac{h^4 y^2}{12}\right) + \partial_x^2 h\left(-\frac{y^5}{120} + \frac{h^3 y^2}{3}\right)\right] \tag{B.2b}$$

Appendix B.3. Second order $O(\varepsilon^2)$

$$
\begin{aligned}
u^{(2)}(h(x,t),y) = {} & \frac{Re^2\,\Lambda\,\varepsilon^2}{We}\,\partial_{xxxx}h\left(\frac{y^6}{360}-\frac{hy^5}{60}+\frac{h^2y^4}{12}-\frac{h^3y^3}{6}+\frac{7h^5y}{30}\right)+\\
&+\frac{Re^2\,\Lambda\,\varepsilon^2}{We}\,\partial_x h\,\partial_{xxx}h\left(\frac{5hy^4}{12}-\frac{3h^2y^3}{2}+\frac{17h^4y}{6}\right)+\\
&+\frac{Re^2\,\Lambda\,\varepsilon^2}{We}\,\partial^2_{xx}h\left(\frac{hy^4}{4}-h^2y^3+2h^4y\right)+\\
&+\frac{Re^2\,\Lambda\,\varepsilon^2}{We}\,\partial^2_x h\,\partial_{xx}h\left(\frac{y^4}{2}-2hy^3+4h^3y\right)+\\
&+\frac{Re^2\,\Lambda\,\cos\beta}{Fr}\,\partial^2_x h\left(-\frac{hy^4}{6}+\frac{h^2y^3}{2}-\frac{5h^4y}{6}\right)+\\
&+\frac{Re^2\,\Lambda\,\cos\beta}{Fr}\,\partial_{xx}h\left(-\frac{y^6}{360}+\frac{hy^5}{60}-\frac{h^2y^4}{12}+\frac{h^3y^3}{6}-\frac{7h^5y}{30}\right)+\\
&+\Lambda\,\partial_{xx}h\left(-\frac{y^3}{3}-\frac{hy^2}{2}+\frac{5h^2y}{2}\right)+\\
&+Re^2\,\Lambda^3\,\partial_{xx}h\left(-\frac{hy^8}{4480}+\frac{h^2y^7}{560}-\frac{h^3y^6}{180}+\frac{h^4y^5}{120}+\frac{h^5y^4}{72}-\frac{h^6y^3}{18}+\frac{29h^8y}{315}\right)+\\
&+Re^2\,\Lambda^3\,\partial^2_x h\left(-\frac{y^8}{4480}+\frac{hy^7}{560}-\frac{7h^2y^6}{720}+\frac{h^3y^5}{30}+\frac{5h^4y^4}{72}-\frac{h^5y^3}{3}+\frac{38h^7y}{63}\right)+\\
&+\Lambda\,\partial^2_x h\left(5hy-\frac{y^2}{2}\right)+\frac{M^2\Lambda\,\cos\beta}{Fr}\left(\frac{y^3}{6}-\frac{hy^2}{2}+\frac{h^2y}{2}\right)
\end{aligned}
\tag{B.3}
$$

Appendix C. Validation with Orr–Sommerfeld problem within the incompressible limit

Our second–order model (25) correctly recovers the expressions for $c^{(0)}$, $c^{(1)}\big|_{Ma\to0^+}$ and $c^{(2)}\big|_{Ma\to0^+}$, which show accordance with the asymptotic expansions of solutions to Orr–Sommerfeld boundary–value problem – reported in Ruyer-Quil and Manneville (1998). However, it is expected that higher–order ex-

$Re\cot^2\beta$	$Re^2\cot\beta$	$\cot\beta$	Re/We	Re^3	Re
-16.7	21.6	-63.0	0	28.9	7.8

Table C.2: Percent errors [%] (expressed to one decimal place) committed by the incompressible evaluation of the present second–order model $(25)|_{Ma\to 0^+}$ in the estimate of polynomial coefficients $\star$ of the $O(k^3)$ incompressible wave celerity $c^{(3)}\big|_{Ma\to 0^+}$, given by $(34\mathrm{d})|_{Ma\to 0^+}$ by comparison with the exact ones (Ruyer-Quil and Manneville, 1998; Chang and Demekhin, 2002) provided by the Orr–Sommerfeld theory.

pressions of $c^{(j)}$ with $j > 2$ are not correctly captured. Specifically, when the incompressible limit of $c^{(3)}$, expressed by $(34\mathrm{d})|_{Ma\to 0^+}$, is contrasted with its exact Orr-Sommerfeld (O–S) analogue, we notice that all terms are present, but with different numerical coefficients in front of them in almost every occurrence $\star$. As shown in table C.2, such discrepancies can be quantified in terms of relative percentage deviation

$$\frac{\star^{(3)}_{(34\mathrm{d})}\Big|_{Ma\to 0^+} - \star^{(3)}_{\text{O–S}}}{\star^{(3)}_{\text{O–S}}} \cdot 100\% \quad [\%]\,. \tag{C.1}$$

A numerical validation of the present second–order weakly–compressible model within its incompressible limit $(25)|_{Ma\to 0^+}$ can be accomplished by comparing its predictions to data from the literature concerning the long–wave interfacial instability for a liquid falling film flow. Figure C.12 compares growth rate and angular frequency of linear surface waves with results of Brevdo et al. (1999) for the case of a liquid film falling down an incline within a passive atmosphere. We remark that agreement is achieved between the two sets of data with reference to the immediate proximity to the limit of infinitely long–wave ($k \to 0^+$), as long as the Reynolds number Re is chosen

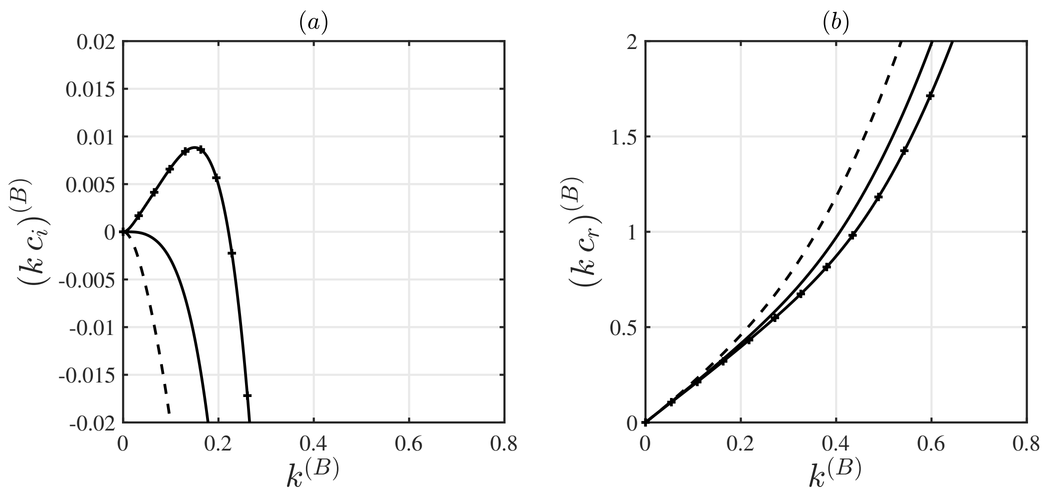

Figure C.12: Comparison of the dimensionless (a) temporal growth rate $k\,c_i(k)$ and (b) angular wave frequency $k\,c_r(k)$ between our work and Brevdo et al. (1999) (figure 2 there). Parameter values: $g = 9.81\,\mathrm{m\,s^{-2}}$, $\beta = 4.6°$, $\tilde{\rho}_0 = 1130\,\mathrm{kg\,m^{-3}}$, $\tilde{\mu}_0 = 5.673\,10^{-3}\,\mathrm{Pa\,s}$, $\tilde{\gamma}_0 = 69.0\,10^{-3}\,\mathrm{N\,m^{-1}}$. Values of the Reynolds number $Re^{(B)} = (3/2)\,Re$ according to Brevdo's scaling: 10 (dashed line), $Re_{cr}^{(B)} = (5/4)\cot\beta$ (bare solid line), 20 (pluses). Note that $k^{(B)}$, $(k\,c_r)^{(B)}$ and $(k\,c_i)^{(B)}$ are scaled as in Brevdo et al. (1999), *i.e.* using the Nusselt film thickness $\tilde{h}_N$ and the free–surface velocity $(3/2)\,\tilde{U}_N$ as length and velocity scales, respectively, instead of the film mean velocity $\tilde{U}_N$ as done here.

to be compliant with the pertinent assumption $Re = O(1)$ made in § 3.

References

Alekseenko, S., Nakoryakov, V., Pokusaev, B., 1985. Wave formation on vertical falling liquid films. International Journal of Multiphase Flow 11, 607–627. doi:10.1016/0301-9322(85)90082-5.

Alekseenko, S., Nakoryakov, V., Pokusaev, B., 1994. Wave flow of liquid films. Begell house.

Almqvist, A., Burtseva, E., Pérez-Ráfols, F., Wall, P., 2019. New insights on lubrication theory for compressible fluids. International Journal of Engineering Science 145, 103170. doi:10.1016/j.ijengsci.2019.103170.

Batchelor, G., 2000. An Introduction to Fluid Dynamics. Cambridge Mathematical Library, Cambridge University Press. doi:10.1017/CBO9780511800955.

Benjamin, T., 1957. Wave formation in laminar flow down an inclined plane. Journal of Fluid Mechanics 2, 554–573. doi:10.1017/S0022112057000373.

Benney, D., 1966. Long waves on liquid films. Journal of Mathematics and Physics 45, 150–155. doi:10.1002/sapm1966451150.

Bresch, D., Cellier, N., Couderc, F., Gisclon, M., Noble, P., Richard, G.L., Ruyer-Quil, C., Vila, J.P., 2020. Augmented skew–symmetric system for shallow–water system with surface tension allowing large gradient of density. J. Comput. Phys. 419, 109670. doi:10.1016/j.jcp.2020.109670.

Brevdo, L., Laure, P., Dias, F., Bridges, T.J., 1999. Linear pulse structure and signalling in a film flow on an inclined plane. J.Fluid Mech. 396, 37–71. doi:10.1017/S0022112099005790.

Cellier, N., Ruyer-Quil, C., 2020. A new family of re duce d models for non-isothermal falling films. International Journal of Heat and Mass Transfer 154, 119700. doi:10.1016/j.ijheatmasstransfer.2020.119700.

Chang, H.C., 1986. Nonlinear waves on liquid film surfaces - i. flooding in a vertical tube. Chemical Engineering Science 41, 2463–2476. doi:10.1016/0009-2509(86)80032-x.

Chang, H.C., 1994. Wave evolution on a falling film. Annual Review of Fluid Mechanics 26, 103–136. doi:10.1146/annurev.fl.26.010194.000535.

Chang, H.C., Demekhin, E., 2002. Complex Wave Dynamics on Thin Films. Elsevier.

Colinet, P., Legros, J.C., Velarde, M.G., 2001. Nonlinear dynamics of surface-tension-driven instabilities. volume 527. Wiley Online Library.

Craster, R.V., Matar, O.K., 2009. Dynamics and stability of thin liquid films. Rev. Mod. Phys. 81, 1131–1198. doi:10.1103/RevModPhys.81.1131.

Dietze, G.F., 2016. On the kapitza instability and the generation of capillary waves. J. Fluid Mech. 789, 368–401. doi:10.1017/jfm.2015.736.

Frisk, D.P., Davis, E.J., 1972. The enhancement of heat transfer by waves in stratified gas–liquid flow. International Journal of Heat and Mass Transfer 15, 1537–1552. doi:10.1016/0017-9310(72)90009-9.

Gjevik, B., 1970. Occurrence of finite-amplitude surface waves on falling liquid films. Physics of Fluids 13, 1918. doi:10.1063/1.1693186.

Jeffreys, H., 1926. XVI. On the relation to physics of the notion of convergence of series. The London, Edinburgh, and Dublin Philosophical Magazine and Journal of Science 2, 241–244.

Kalliadasis, S., Ruyer-Quil, C., Scheid, B., Velarde, M., 2013. Falling Liquid Films. Springer.

Kapitza, P.L., 1948. Wave flow of thin layers of a viscous fluid: I. free flow., in: Haar, D.T. (Ed.), Collected Papers of P. L. Kapitza (1965). Pergamon, pp. 662–679. (Original paper in Russian: Zh. Ekper. Teor. Fiz., 18, I. 3–18).

Kapitza, P.L., Kapitza, S.P., 1949. Wave flow of thin fluid layers of liquid., in: Haar, D.T. (Ed.), Collected Papers of P. L. Kapitza (1965). Pergamon, pp. 662–679. (Original paper in Russian: Zh. Ekper. Teor. Fiz., 19: 105–120).

Kelly, R.E., Goussis, D.A., Lin, S.P., Hsu, F.K., 1989. The mechanism for surface wave instability in film flow down an inclined plane. Phys. Fluids A 1, 819–826.

Kinsler, L., Frey, A., Coppens, A., Sanders, J., 2000. Absorption and Attenuation of Sound. John Wiley & Sons, New York. p. 210–245.

Lavalle, G., Li, Y., Mergui, S., Grenier, N., Dietze, G.F., 2019. Suppression of the kapitza instability in confined falling liquid films. J. Fluid Mech. 860, 608–639. doi:10.1017/jfm.2018.902.

Lavalle, G., Vila, J.P., Blanchard, G., Laurent, C., Charru, F., 2015. A numerical reduced model for thin liquid films sheared by a gas flow. Journal of Computational Physics 301, 119–140. doi:10.1016/j.jcp.2015.08.018.

Lavalle, G., Vila, J.P., Lucquiaud, M., Valluri, P., 2017. Ultraefficient reduced model for countercurrent two-layer flows. Phys. Rev. Fluids 2, 014001. doi:10.1103/PhysRevFluids.2.014001.

Lin, S., 1974. Finite amplitude side-band stability of a viscous film. Journal of Fluid Mechanics 63, 417–429. doi:10.1017/s0022112074001704.

Liu, J., Gollub, J., 1994. Solitary wave dynamics of film flows. Physics of Fluids 6, 1702–1712. doi:10.1063/1.868232.

Lu, H., Ma, X., Huang, K., Fu, L., Azimi, M., 2020. Carbon dioxide transport via pipelines: A systematic review. Journal of Cleaner Production 266, 121994. doi:10.1016/j.jclepro.2020.121994.

Meliga, P., Sipp, D., Chomaz, J.M., 2010. Effect of compressibility on the global stability of axisymmetric wake flows. Journal of Fluid Mechanics 660, 499–526. doi:10.1017/S002211201000279X.

Noble, P., Vila, J.P., 2013. Thin power-law film flow down an inclined plane: consistent shallow-water models and stability under large-scale perturbations. Journal of Fluid Mechanics 735, 29–60. doi:10.1017/jfm.2013.454.

Noble, P., Vila, J.P., 2014. Stability theory for difference approximations of euler–korteweg equations and application to thin film flows. SIAM Journal on Numerical Analysis 52, 2770–2791. doi:10.1137/130918009.

Nusselt, W., 1916. Die oberflachenkondensation des wasserdampfes. Z. Verein. Deutsch. Ing. 50, 541–546.

Ooshida, T., 1999. Surface equation of falling film flows with moderate Reynolds number and large but finite Weber number. Physics of Fluids 11, 3247–3269. doi:10.1063/1.870186.

Orr, W.M., 1907. The stability or instability of the steady motions of a perfect liquid and of a viscous liquid. part ii: a viscous liquid. Proc. Roy. Irish Acad. 27, 69–138. doi:10.2307/20490591.

Richard, G., 2021. An extension of the boussinesq-type models to weakly compressible flows. European Journal of Mechanics - B/Fluids 89, 217–240. doi:10.1016/j.euromechflu.2021.05.011.

Richard, G., Gisclon, M., Ruyer-Quil, C., Vila, J., 2019. Optimization of consistent two-equation models for thin film flows. European Journal of Mechanics - B/Fluids 76, 7–25. doi:10.1016/j.euromechflu.2019.01.004.

Richard, G., Ruyer-Quil, C., Vila, J., 2016. A three-equation model for thin films down an inclined plane. Journal of Fluid Mechanics 804, 162–200. doi:10.1017/jfm.2016.530.

Ruyer-Quil, C., 2012. Instabilities and modeling of falling film flows. Fluids mechanics [physics.class-ph], Université Pierre et Marie Curie - Paris VI. p. 285. URL: `https://theses.hal.science/tel-00746483`.

Ruyer-Quil, C., Manneville, P., 1998. Modeling film flows down inclined planes. The European Physical Journal B 6, 277–292. doi:10.1007/s100510050550.

Ruyer-Quil, C., Manneville, P., 2000. Improved modeling of flows down inclined planes. The European Physical Journal B 15, 357–369. doi:10.1007/s100510051137.

Ruyer-Quil, C., Manneville, P., 2002. Further accuracy and convergence results on the modeling of flows down inclined planes by weighted-residual approximations. Physics of Fluids 14, 170–183. doi:10.1063/1.1426103.

Ruyer-Quil, C., Treveleyan, P., Giorgiutti-Dauphiné, F., Duprat, C., Kalliadasis, S., 2008. Modelling film flows down a fibre. J. Fluid Mech. 603, 431—462. doi:10.1017/S0022112008001225.

Samanta, A., 2014. Shear-imposed falling film. Journal of Fluid Mechanics 753, 131–149. doi:10.1017/jfm.2014.351.

Samanta, A., Ruyer-Quil, C., Goyeau, B., 2011. A falling film down a slippery inclined plane. Journal of Fluid Mechanics 684, 353–383. doi:10.1017/jfm.2011.304.

Shapiro, A.H., 1953. The Dynamics and Thermodynamics of Compressible Fluid Flow. volume 1. John Wiley & Sons, New York.

Sharma, A., Dandapat, B.S., 2006. Wave Dynamics and Stability of Thin Film Flow Systems. Alpha Science Int'l Ltd.

Shkadov, V.Y., 1967. Wave flow regimes of a thin layer of viscous fluid subject to gravity. Izv. Akad. Nauk SSSR Mekh. Zhidk. Gaza 1, 43–51. doi:10.1007/bf01024797. (translation in 1970 *Fluid Dyn.* **2**, 29–34).

Simmonds, J.G., Mann Jr, J.E., 1998. A first look at perturbation theory. Courier Corporation.

Smith, M.K., 1990. The mechanism for the long-wave instability in thin liquid films. J. Fluid Mech. 217, 469–485.

Sommerfeld, A., 1908. Ein beitrag zur hydrodynamischen erklarung der turbulenten flussigkeisbewegung. Atti Congr. Int. Math. 4th .

Thompson, A.B., Gomes, S.N., Denner, F., Dallaston, M.C., Kalliadasis, S., 2019. Robust low-dimensional modelling of falling liquid films subject to variable wall heating. Journal of Fluid Mechanics 877, 844–881. doi:10.1017/jfm.2019.580.

Trevelyan, P.M.J., Scheid, B., Ruyer-Quil, C., Kalliadasis, S., 2007. Heated falling films. Journal of Fluid Mechanics 592, 295–334. doi:10.1017/S0022112007008476.

Van Dael, W., 1968. Thermodynamic Properties and the Velocity of Sound. Springer US, Boston, MA. pp. 527–577. doi:10.1007/978-1-4899-6569-1-17.

Van Dyke, M., Rosenblat, S., 1975. Perturbation method in fluid mechanics. The Parabolic Press.

Weinstein, S.J., Ruschak, K.J., 2004. Coating flows. Annu. Rev. Fluid Mech. 36, 29–53. doi:10.1146/annurev.fluid.36.050802.122049.

Whitham, G., 1974. Linear and Nonlinear Waves. Wiley–Interscience.

Yih, C.S., 1963. Stability of liquid flow down an inclined plane. Physics of Fluids 6, 321. doi:10.1063/1.1706737.